

## An efficient explicit–implicit adaptive method for peridynamic modeling of quasi-static fracture formation and evolution

Shiwei Hu <sup>a</sup>, Tianbai Xiao <sup>a,b</sup>, Mingshuo Han <sup>a,b</sup>, Zuoxu Li <sup>a,b</sup>, Erkan Oterkus <sup>c</sup>, Selda Oterkus <sup>c</sup>, Yonghao Zhang <sup>a,b</sup>,<sup>\*</sup>

<sup>a</sup> Centre for Interdisciplinary Research in Fluids, Institute of Mechanics, Chinese Academy of Sciences, Beijing, 100190, China

<sup>b</sup> School of Engineering Science, University of Chinese Academy of Sciences, Beijing, 100049, China

<sup>c</sup> Department of Naval Architecture, Ocean, and Marine Engineering, University of Strathclyde, Glasgow, G1 1QN, United Kingdom

### ARTICLE INFO

**Keywords:**  
 Peridynamics  
 Quasi-static fracture mechanics  
 Computational mechanics  
 Implicit method  
 Explicit ADR

### ABSTRACT

Understanding the quasi-static fracture formation and evolution is essential for assessing the mechanical properties and structural load-bearing capacity of materials. Peridynamics (PD) provides an effective computational method to depict fracture mechanics. The explicit adaptive dynamic relaxation (ADR) method and the implicit methods are two mainstream PD approaches to simulate evolution of quasi-static fractures. However, no comprehensive and quantitative studies have been reported to compare their accuracy and efficiency. In this work, we first develop an implicit method for bond-based peridynamics (BBPD) based on the full nonlinear equilibrium equation and the degenerate form of the bond failure function, where the Jacobian matrices are derived using the Newton–Raphson (NR) scheme. Subsequently, we analyze the solvability of the implicit BBPD scheme. Second, a consistent and comprehensive comparison of accuracy and efficiency of the explicit ADR and implicit methods is conducted, which reveals computational efficiency of the implicit methods and their limitations in accurately describing crack formation. Finally, by utilizing the unique advantage of both methods, we develop an adaptive explicit–implicit method and propose a switching criterion to deploy appropriate scheme accordingly. Four typical quasi-static problems are employed as the numerical experiments, which show the acceleration ratios of the current method range from 6.4 to 141.7 when compared to the explicit ADR. Therefore, the explicit–implicit adaptive method provides a powerful method to simulate quasi-static fracture formation and evolution.

### 1. Introduction

Peridynamics (PD) offers an alternative method for modeling and simulation of fracture behavior [1–7], which has made rapid progress in the recent years. Unlike classical continuum mechanics (CCM) that relies on differential operators, PD models the evolution of materials using non-local interactions between the material points within a finite distance. Thus, it naturally mitigates the well-posedness issue of the derivatives appearing at cracks and voids. Both continuous and discontinuous fields can be solved within the same framework, where cumbersome remedial techniques are not required [8–18]. Based on modeling of non-local interactions, PD can be divided into two categories, i.e., bond-based PD (BBPD) and state-based PD (SBPD) methods. It is worth mentioning that there is a special type of PD model, dual-horizon peridynamics (DH-PD). By introducing the dual horizon concept,

\* Corresponding author at: Centre for Interdisciplinary Research in Fluids, Institute of Mechanics, Chinese Academy of Sciences, Beijing, 100190, China.  
 E-mail address: [yonghao.zhang@imech.ac.cn](mailto:yonghao.zhang@imech.ac.cn) (Y. Zhang).

<b>Nomenclature</b>	
Symbols	Physical quantities, units
$\mathbf{x}$	Position vector before deformation, unit: m
$\mathbf{y}$	Position vector after deformation, unit: m
$\mathbf{u}, \ddot{\mathbf{u}}$	Displacement vector, unit: m, acceleration vector, unit: m/s <sup>2</sup>
$\xi, \eta$	Relative position vector, relative displacement vector, unit : m
$\mathbf{f}(\mathbf{u}' - \mathbf{u}, \mathbf{x}' - \mathbf{x}, t)$	Interaction force density vector between the particles at $\mathbf{x}'$ and $\mathbf{x}$ at the time $t$ , unit: N/m <sup>3</sup>
$\mathbf{F}(\xi, \mathbf{u})$	Set of the total interaction force density vectors acting on each PD point in the entire material, unit: N/m <sup>3</sup>
$\mathbf{b}$	Volumetric body force density vector, unit: N/m <sup>3</sup>
$c$	Bond constant, unit: Pa/m <sup>4</sup>
$s$	Bond stretch
$\rho$	Density, unit: Kg/m <sup>3</sup>
$E$	Young's modulus, unit: Pa
$N$	Total number of particles in the computed materials
$N_i$	Number of particles within the horizon $H_i$
$\Delta\mathbf{u}_m$	Displacement increment vector, unit: m
$\mathbf{K}$	Jacobian matrix
$e$	Relative error tolerance of the NR procedure
$e_0$	Relative error tolerance of the whole-field displacement
$S$	Sparsity index
$\Delta x$	Spatial discretization size, unit: m
$T_s$	Degradation function
$s_m$	Minimum bond stretch for bond interaction degradation
$s_c$	Critical bond stretch
$l, w, h$	Length, width, height, unit: m
$\Delta u_i$	Displacement loading increments for the implicit scheme, unit: m
$\Delta u_e$	Displacement loading increments for the explicit scheme, unit: m
$u_{total}$	Total displacement loading, unit: m
$N_i$	Total implicit loading steps to reach the total displacement
$N_e$	Total explicit loading steps to reach the total displacement
$r_a$	Acceleration ratio of the adaptive method in comparison to the explicit-ADR method
$r_h$	Ratio of the duration of the deformation stage to the total simulation duration

it has a varying horizon size to resolve the “ghost force” issue, and enables the adaptive refinement method [19,20]. The PD in DH-PD framework can also be classified into BBPD and SBPD.

BBPD models the interaction between material points as the force of equal magnitude pointing to the opposite directions along the interaction direction [9]. Despite the limitation of fixed Poisson’s ratio, BBPD models are widely used in the modeling of brittle materials due to the favorable numerical stability, succinct mathematical form and low computational cost, and effectiveness in addressing multi-physical coupling problems [21–37]. Therefore, this study will focus on the BBPD, and may be extended to SBPD in the future.

Quasi-static problems are vital in the study of engineering structural deformation, subsurface movement and deformation, material performance testing, and loading assessment [38–45]. Although PD has been successfully applied to simulate dynamic fracture propagation [40,41,43,46–48], obtaining steady-state solutions under quasi-static conditions remains challenging [38]. This difficulty arises due to the fact that the small time step employed in the explicit time integrators leads to overwhelmingly-costly computation. To address this issue, Kilic et al. [38] extended the adaptive dynamic relaxation (ADR) method to PD simulation, where the damping coefficient in dynamic relaxation was estimated using Rayleigh’s quotient to effectively dampen the system from higher frequency modes to lower frequency modes. This explicit-ADR method can achieve steady-state solutions under quasi-static conditions and accurately capture fracture propagation. However, small loading rates are necessary to avoid nonphysical force fluctuations caused by dynamic effects.

On the other hand, the implicit PD schemes have been proposed for static or quasi-static problems [39,49–55], which allow larger loading steps, faster convergence, and guaranteed equilibrium conditions. Among others, Breitenfeld et al. [55] presented the development of a static implementation for the non-ordinary state-based PD (NOSBPD) formulation, focusing on small-strain linearly elastic problems. Ni et al. [52] proposed an implicit form of the finite element method (FEM)-BBPD coupled model to address static fracture problems and introduced three methods to compute crack propagation, i.e., allowing only one bond to break per step, no control of bond breakage, and limiting the maximum number of bonds that can break at each step. It turned out that

the third method significantly improved the accuracy of numerical solution. The linearized equilibrium equation was used in that model under the small displacement assumption [1,56]. Gu et al. [37] also applied such linearized equilibrium equation of BBPD within their framework to study porous quasi-brittle materials. If the linearized PD equation is used, small loading increments are required to ensure that the displacements remain sufficiently small at each step to satisfy the prerequisite for linearization, i.e., small deformation.

To remove the small deformation restriction, the full nonlinear form of PD is favored in conjunction with iterative schemes such as the Newton–Raphson (NR). However, the three mainstream crack computation methods discussed above are not suitable for the NR procedure due to the fact that, when there are cracks, the force field becomes discontinuous, making it difficult to obtain the Jacobian matrix. Hashim et al. [50] proposed an implicit NOSBPD framework using the NR scheme, where a degradation function is introduced to describe damage evolution, i.e., the interaction degradation of the bond as the bond stretch increases, which is different from immediate disappearance of the bond influence. Yang et al. [49] improved the implicit NOSBPD model by incorporating a stress-based criterion to evaluate bond failure, which overcame the difficulties associated with obtaining fracture properties in the previous critical stretch criterion. While the implicit schemes for NOSBPD have been studied, the detailed implementation for BBPD, which is equally crucial, has not garnered adequate attention yet. Also, since implicit methods aim to reduce computational costs, it is necessary to compare the computational efficiency between the explicit-ADR and implicit schemes for quasi-static problems, which has not been systematically examined.

Here, we first develop an implicit method based on the full nonlinear equilibrium equation and the degenerate form of the bond failure function of BBPD for quasi-static problems. The Jacobian matrix is obtained using the NR scheme, which lays the foundation for the implicit scheme. We thoroughly compare the computational efficiency and accuracy of the explicit-ADR method and the newly-developed implicit method. Leveraging the advantages of both methods, we propose an explicit–implicit adaptive method that strikes a balance between accuracy and efficiency for quasi-static fracture problems. The performance of the adaptive method will be elaborated for four quasi-static problems.

Note that although implicit schemes were reported in the literature [37,49,50,52,55], the novel contributions of this work lie in two key aspects. First, the nonlinear form of the BBPD equation is retained to eliminate the small-strain restriction often encountered in BBPD studies [1,37,38,52,53,56]. More importantly, this study presents the first comprehensive comparison of two mainstream methods, i.e., the explicit ADR and implicit schemes, for quasi-static problems. Based on this comparison, a new adaptive scheme is proposed that effectively combines the advantages of both approaches. Additionally, the current efficient adaptive scheme is also applicable to SBPD.

The rest of the paper is organized as follows. Section 2 introduces BBPD and presents a new implicit model for quasi-static problems. Section 3 provides a comprehensive comparison between the explicit-ADR method and the newly-developed implicit method. Section 4 details a novel explicit–implicit adaptive method tailored for quasi-static fracture problems. Following this, Section 5 highlights four typical case studies, revealing the computational accuracy and efficiency of the explicit–implicit adaptive method. The conclusions and further discussion on the remaining issues are presented in the last section.

## 2. Theoretical model

In this section, we formulate a new implicit BBPD method for quasi-static problems. The nonlinear equilibrium equation is analyzed by examining the properties of the Jacobian matrix, and the degradation of bond damage is illustrated.

### 2.1. Implicit formulation of full nonlinear BBPD model

The equation of motion of BBPD is given by

$$\rho(\mathbf{x})\ddot{\mathbf{u}}(\mathbf{x}, t) = \int_H \mathbf{f}(\mathbf{u}' - \mathbf{u}, \mathbf{x}' - \mathbf{x}, t) dH + \mathbf{b}(\mathbf{x}, t), \quad (1)$$

where  $H$  represents the horizon zone of the particle at the position  $\mathbf{x}$ ,  $\mathbf{f}(\mathbf{u}' - \mathbf{u}, \mathbf{x}' - \mathbf{x}, t)$  is the force density vector between the particles at  $\mathbf{x}'$  and  $\mathbf{x}$ , both at the time  $t$ ,  $(\mathbf{x}' - \mathbf{x})$  represents the initial relative position vector between the particles at  $\mathbf{x}'$  and  $\mathbf{x}$  in the horizon  $H$ ,  $\mathbf{b}$  is the body force density vector at the time  $t$ ,  $\rho(\mathbf{x})$  presents the mass density of the particle at  $\mathbf{x}$ , and  $\ddot{\mathbf{u}}$  is the second-order time derivative of displacement  $\mathbf{u}$ .

The initial relative position vector  $\xi$  and relative displacement vector  $\eta$  are denoted by  $\xi = \mathbf{x}' - \mathbf{x}$  and  $\eta = \mathbf{u}' - \mathbf{u}$ , where  $\mathbf{u}'$  and  $\mathbf{u}$  are, respectively, the displacement of the particles at  $\mathbf{x}'$  and  $\mathbf{x}$ . After the configuration deformation, the new positions of the particles at  $\mathbf{x}'$  and  $\mathbf{x}$  are represented by  $\mathbf{y}'$  and  $\mathbf{y}$ , where  $\mathbf{y}' = \mathbf{x}' + \mathbf{u}'$  and  $\mathbf{y} = \mathbf{x} + \mathbf{u}$ . The relative positional relationship between the particles  $\mathbf{x}$  and  $\mathbf{x}'$  is depicted in Fig. 1.

The PD integral-form equation can be discretized for numerical implementation as

$$\rho(\mathbf{x}_i)\ddot{\mathbf{u}}(\mathbf{x}_i, t) = \sum_{j=1}^{N_i} [\mathbf{f}_{i,j}(\mathbf{u}_j - \mathbf{u}_i, \mathbf{x}_j - \mathbf{x}_i, t) \mu_{i,j} v_{i,j} V_j] + \mathbf{b}(\mathbf{x}_i, t), \quad (2)$$

where  $N_i$  represents the number of particles within the horizon of the particle located at  $\mathbf{x}_i$ . The subscript  $j$  denotes an arbitrary particle positioned at  $\mathbf{x}_j$  within the horizon of the particle at  $\mathbf{x}_i$ .  $V_j$  is the volume of the particle at  $\mathbf{x}_j$  within the horizon of the particle at  $\mathbf{x}_i$ , given by  $V_j = (\Delta x)^3$  for a uniform discretization. Here,  $v_{i,j}$  and  $\mu_{i,j}$  are the volume and surface effect correction factors for the particle at  $\mathbf{x}_j$  within the horizon of the particle at  $\mathbf{x}_i$ , respectively, and  $\Delta x$  represents the particle spacing.

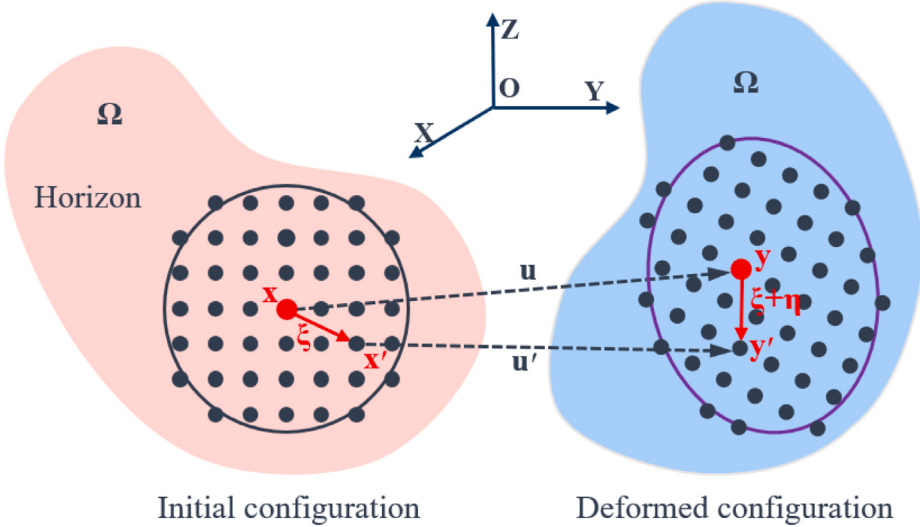


**Fig. 1.** Illustration of BBPD and pairwise interaction between PD points. The horizon of the particle at the position  $x$  encompasses all the PD particles interacting with it, and remains unchanged throughout deformation.

Based on the BBPD theory, the force density vector of each bond  $\mathbf{f}_{ij}$  satisfies

$$\begin{aligned} \mathbf{f}_{ij}(\mathbf{u}_j - \mathbf{u}_i, \mathbf{x}_j - \mathbf{x}_i, t) &= cs \frac{\xi_{ij} + \eta_{ij}}{|\xi_{ij} + \eta_{ij}|} \\ &= c \frac{|\xi_{ij} + \eta_{ij}| - |\xi_{ij}|}{|\xi_{ij}|} \frac{\xi_{ij} + \eta_{ij}}{|\xi_{ij} + \eta_{ij}|} \\ &= c \frac{|\mathbf{y}_j - \mathbf{y}_i| - |\mathbf{x}_j - \mathbf{x}_i|}{|\mathbf{x}_j - \mathbf{x}_i|} \frac{\mathbf{y}_j - \mathbf{y}_i}{|\mathbf{y}_j - \mathbf{y}_i|}, \end{aligned} \quad (3)$$

where  $c$  is bond constant,

$$c = \begin{cases} \frac{2E}{\pi \delta^2 A} & \text{for } 1\text{D}, \\ \frac{9E}{\pi \delta^3 h} & \text{for plane stress,} \\ \frac{48E}{5\pi \delta^3 h} & \text{for plane strain,} \\ \frac{12E}{\pi \delta^4} & \text{for 3D,} \end{cases}$$

and  $s$  is the bond stretch, which is  $s = (|\xi_{ij} + \eta_{ij}| - |\xi_{ij}|)/|\xi_{ij}|$ .

For the quasi-static deformation, the second-order time derivative of displacement can be ignored, the governing equation of BB-PD is given below,

$$\sum_{j=1}^{N_i} c \frac{|\xi_{ij} + \eta_{ij}| - |\xi_{ij}|}{|\xi_{ij}|} \frac{\xi_{ij} + \eta_{ij}}{|\xi_{ij} + \eta_{ij}|} \mu_{i,j} v_{i,j} V_j + \mathbf{b}(\mathbf{x}_i, t) = 0. \quad (4)$$

We propose an implicit algorithm to solve the quasi-static motion equation, thereby avoiding the significant computational cost associated with excessively small time steps required in the explicit time integration. Moreover, the NR scheme is applied to iteratively solve the aforementioned full nonlinear equation.

The function  $E(\mathbf{u})$  is defined as  $E(\mathbf{u}) = \mathbf{F}(\xi, \mathbf{u}) + \mathbf{b}(\mathbf{x})$ , where the function  $\mathbf{F}$  represents the set of the total interaction force density vectors acting on each PD point in the entire material. For the PD point located at  $\mathbf{x}_i$ , one element of  $\mathbf{F}$ , the total interaction force density vector at  $\mathbf{x}_i$ , can be expressed as:

$$\mathbf{F}_i(\xi, \mathbf{u}) = \sum_{j=1}^{N_i} c \frac{|\xi_{ij} + \eta_{ij}| - |\xi_{ij}|}{|\xi_{ij}|} \frac{\xi_{ij} + \eta_{ij}}{|\xi_{ij} + \eta_{ij}|} \mu_{i,j} v_{i,j} V_j.$$

The system reaches equilibrium when the value of  $E(\mathbf{u})$  approaches zero.

According to the NR iteration scheme shown in Fig. 2, expand the function  $E(\mathbf{u})$  at  $\mathbf{u}_m$  using the Taylor series and retain the linear term yields  $E(\mathbf{u}) \approx E(\mathbf{u}_m) + \frac{\partial E}{\partial \mathbf{u}}(\mathbf{u}_m)(\mathbf{u} - \mathbf{u}_m)$ , where  $\mathbf{u}_m$  represents the displacement of the current  $m$  iteration step. The solution to

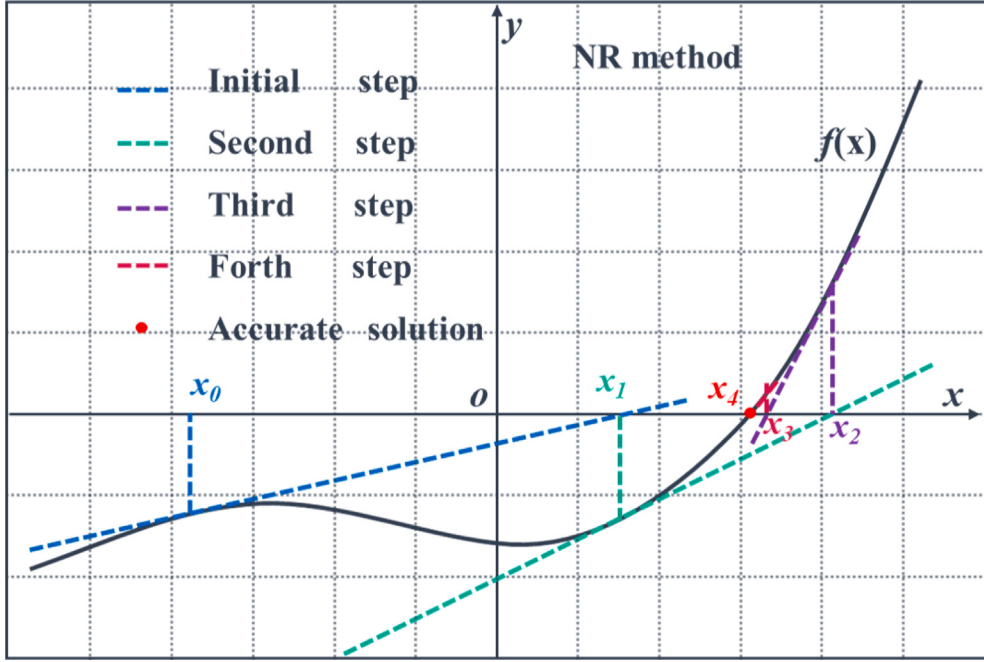


**Fig. 2.** Illustration of the NR procedure: the solution of a nonlinear system equals the zero point of the nonlinear function, and the numerical solution obtained through the NR iteration gradually converges toward the accurate solution.

the nonlinear system  $\mathbf{E}(\mathbf{u}) = \mathbf{0}$  can be transformed into solving the following linear equation at each iteration step,

$$\mathbf{K}_m (\Delta \mathbf{u}_m) = -\mathbf{E} (\mathbf{u}_m), \quad \mathbf{K}_m = \frac{\partial \mathbf{E}}{\partial \mathbf{u}} (\mathbf{u}_m), \quad (5)$$

where  $\mathbf{K}_m$  is the Jacobian matrix (or tangent stiffness matrix) at the  $m$ th iteration, and  $\Delta \mathbf{u}_m = \mathbf{u}_{m+1} - \mathbf{u}_m$  is the unknown displacement increment. Once  $\Delta \mathbf{u}_m$  is determined, the next displacement  $\mathbf{u}_{m+1}$  is updated as  $\mathbf{u}_{m+1} = \mathbf{u}_m + \Delta \mathbf{u}_m$ . This iterative process continues until  $\mathbf{u}_{m+1}$  converges to the required accuracy.

Although  $\mathbf{K}_m$  can be determined numerically [54], the calculation involves finite differencing of the whole-field function  $\mathbf{E}(\mathbf{u})$  with respect to the displacements of all PD points (as shown in Eq. (5)), resulting in significant computational and memory costs. Furthermore,  $\mathbf{K}_m$  changes with each iteration, solving it numerically becomes increasingly expensive. To reduce the computational cost, the analytical expression of  $\mathbf{K}$  can be obtained as,

$$\mathbf{K} = \frac{\partial \mathbf{E}}{\partial \mathbf{u}} = \frac{\partial \mathbf{F}(\xi, \mathbf{u})}{\partial \mathbf{u}} = \begin{bmatrix} \frac{\partial F_1(\xi, \mathbf{u})}{\partial u_1} & \frac{\partial F_1(\xi, \mathbf{u})}{\partial u_2} & \dots & \frac{\partial F_1(\xi, \mathbf{u})}{\partial u_n} \\ \frac{\partial F_2(\xi, \mathbf{u})}{\partial u_1} & \frac{\partial F_2(\xi, \mathbf{u})}{\partial u_2} & \dots & \frac{\partial F_2(\xi, \mathbf{u})}{\partial u_N} \\ \vdots & \vdots & \ddots & \vdots \\ \frac{\partial F_N(\xi, \mathbf{u})}{\partial u_1} & \frac{\partial F_N(\xi, \mathbf{u})}{\partial u_2} & \dots & \frac{\partial F_N(\xi, \mathbf{u})}{\partial u_N} \end{bmatrix}_{N \times N}, \quad (6)$$

where  $\mathbf{K}$  represents the Jacobian matrix function at arbitrary time and  $N$  represents the total number of particles of the material. For three dimensions, the  $3 \times 3$  matrix is given by

$$\frac{\partial \mathbf{F}_i(\xi, \mathbf{u})}{\partial \mathbf{u}_j} = \begin{bmatrix} \frac{\partial F_{ix}(\xi, \mathbf{u})}{\partial u_{jx}} & \frac{\partial F_{ix}(\xi, \mathbf{u})}{\partial u_{jy}} & \frac{\partial F_{ix}(\xi, \mathbf{u})}{\partial u_{jz}} \\ \frac{\partial F_{iy}(\xi, \mathbf{u})}{\partial u_{jx}} & \frac{\partial F_{iy}(\xi, \mathbf{u})}{\partial u_{jy}} & \frac{\partial F_{iy}(\xi, \mathbf{u})}{\partial u_{jz}} \\ \frac{\partial F_{iz}(\xi, \mathbf{u})}{\partial u_{jx}} & \frac{\partial F_{iz}(\xi, \mathbf{u})}{\partial u_{jy}} & \frac{\partial F_{iz}(\xi, \mathbf{u})}{\partial u_{jz}} \end{bmatrix}_{3 \times 3}, \quad (7)$$

where the subscript  $x$ ,  $y$ , and  $z$  represent three mutually orthogonal Cartesian coordinate components, respectively.

If we substitute Eq. (7) into Eq. (6) for  $j \neq i$ , and the particle at the position  $\mathbf{x}_j$  belongs to the horizon of the particle at the position  $\mathbf{x}_i$ , i.e.,  $\mathbf{x}_j \in H_i$ , we obtain

$$\frac{\partial F_{ip}(\xi, \mathbf{u})}{\partial u_{jq}} = c \mu_{i,j} v_{i,j} V_j \left[ \frac{\delta_{pq}}{|\mathbf{x}_j - \mathbf{x}_i|} - \frac{\delta_{pq}}{|\mathbf{y}_j - \mathbf{y}_i|} + \frac{(y_{jp} - y_{ip})(y_{jq} - y_{iq})}{|\mathbf{y}_j - \mathbf{y}_i|^3} \right], \quad (8)$$

where the subscripts  $i$  and  $j$  represent the coordinate indices ( $i, j = 1, 2, \dots, N$ ), and  $p$  and  $q$  denote the indices for the orthogonal component directions of the position vectors ( $p, q = x, y, z$ ). For example,  $y_{jp}$  represents the position coordinate component of particle  $j$  in the  $p$  direction after deformation.  $\delta_{pq} = 1$  when  $p = q$ , and  $\delta_{pq} = 0$  otherwise.

If  $j \neq i$  and the particle at the position  $\mathbf{x}_j$  does not belong to the horizon of the particle at the position  $\mathbf{x}_i$ , i.e.,  $\mathbf{x}_j \notin H_i$ , we can obtain

$$\frac{\partial \mathbf{F}_i(\xi, \mathbf{u})}{\partial \mathbf{u}_j} = \mathbf{0}. \quad (9)$$

If  $j = i$ , similarly, we obtain

$$\frac{\partial F_{ip}(\xi, \mathbf{u})}{\partial u_{iq}} = c \sum_{\mathbf{x}_k \in H_i} \left[ \frac{\delta_{pq}}{|\mathbf{y}_k - \mathbf{y}_i|} - \frac{\delta_{pq}}{|\mathbf{x}_k - \mathbf{x}_i|} - \frac{(y_{kp} - y_{ip})(y_{kq} - y_{iq})}{|\mathbf{y}_k - \mathbf{y}_i|^3} \right] \mu_{i,k} v_{i,k} V_k, \quad (10)$$

where the subscript  $k$  represents the coordinate indices, and  $k = 1, 2, \dots, N$ .

In summary, the dimension of Jacobian matrix  $\mathbf{K}$  is  $mN \times mN$ , where  $m$  represents the dimension of the system ranging from 1 to 3. Each element of the Jacobian matrix  $\mathbf{K}$  can be calculated by Eqs. (6)–(10).

In the same manner, the right-hand side of Eq. (5), which is a  $mN \times 1$  vector, can be calculated by

$$-E(u_{ip}) = c \sum_{\mathbf{x}_k \in H_i} \left[ \frac{(y_{kp} - y_{ip})}{|\mathbf{y}_k - \mathbf{y}_i|} - \frac{(y_{kp} - y_{ip})}{|\mathbf{x}_k - \mathbf{x}_i|} \right] \mu_{i,k} v_{i,k} V_k - b_{ip}, \quad (11)$$

$$(i, k = 1, 2 \dots N; p, q = x, y, z).$$

By solving the linear system,  $\Delta \mathbf{u}_m$  can be obtained, and the displacement of the next step is  $\mathbf{u}_{m+1} = \mathbf{u}_m + \Delta \mathbf{u}_m$ . The convergence criterion of the NR procedure is set as  $\frac{\|E(\mathbf{u}_{m+1})\|_2}{\|b(\xi)\|_2} \leq e$ , where  $e$  stands for the relative error tolerance.

## 2.2. Properties of Jacobian matrix for implicit BBPD model

The typical Jacobian matrix of BBPD for quasi-static problems exhibits the following properties.

(1) Sparsity: the number of non-zero elements in  $\mathbf{K}$  is associated with the total number of particles in a horizon. The sparsity index  $S$  can be calculated as  $S = \sum_{i=1}^N (N_i + 1)/N^2$ , where  $(N_i + 1)$  represents the total number of particles in the horizon of particle  $i$ , including itself. Furthermore, not all horizons contain the same number of particles due to the presence of surfaces, so  $S < \frac{N_m + 1}{N}$ , where  $N_m$  is the maximum number of localized particles, which is typically constant in PD simulations. As the horizon size is commonly set to be  $3\Delta x$ , the value of  $N_m$  is typically equal to 3 for 1-dimensional (1D) problems, 28 for 2D problems, and 122 for 3D problems. Therefore,  $\mathbf{K}$  is sparse as  $N \gg N_m$ .

(2) Symmetry: if we take the 3D Jacobian matrix  $\mathbf{K}$  as an example, each element of  $\mathbf{K}_{3N \times 3N}$  can be expressed as  $[K_{i,j}]_{p,q}$ , where  $i$  and  $j$  represent the index numbers of all the particles, and  $p$  and  $q$  represent the axis components of the Cartesian coordinate.

If  $j \neq i$ , from Eq. (8), we obtain

$$[K_{i,j}]_{p,q} = c \mu_{i,j} v_{i,j} V_j \left[ \frac{\delta_{pq}}{|\mathbf{x}_j - \mathbf{x}_i|} - \frac{\delta_{pq}}{|\mathbf{y}_j - \mathbf{y}_i|} + \frac{(y_{jp} - y_{ip})(y_{jq} - y_{iq})}{|\mathbf{y}_j - \mathbf{y}_i|^3} \right],$$

$$[K_{j,i}]_{q,p} = c \mu_{i,j} v_{i,j} V_i \left[ \frac{\delta_{pq}}{|\mathbf{x}_i - \mathbf{x}_j|} - \frac{\delta_{pq}}{|\mathbf{y}_i - \mathbf{y}_j|} + \frac{(y_{iq} - y_{ij})(y_{ip} - y_{jp})}{|\mathbf{y}_i - \mathbf{y}_j|^3} \right].$$

In PD simulations, the grids are usually uniform, which mean  $V_j = V_i$ , so that,  $[K_{i,j}]_{p,q} = [K_{j,i}]_{q,p}$ . If  $j = i$ , the elements are on the diagonal of a square matrix, so  $[K_{i,i}]_{p,q} = [K_{i,i}]_{q,p}$ . Therefore,  $\mathbf{K}$  is a symmetric matrix.

(3) Other important property: as for the diagonal elements of the particle index matrix  $[K_{i,i}]$ , the arbitrary Cartesian coordinate components  $[K_{i,i}]_{p,q}$  can be expressed as Eq. (10), and we get  $[K_{i,i}]_{p,q} = -\sum_{j=1}^{N_i} [K_{i,j}]_{p,q}$ . This implies that  $\mathbf{K}$  is a matrix with the row sum equal to 0. Therefore,  $\mathbf{K}$  is singular and requires the introduction of boundary condition to eliminate singularity.

To be more illustrative, we compute a specific Jacobian matrix for a particular quasi-static case before applying boundary conditions. This case involves a 2D bar subjected to a transverse loading, which will be discussed in Section 3.1. Fig. 3 displays the distribution of non-zero elements in this Jacobian matrix. As for the positive definiteness of the Jacobian matrix, the theoretical proof is yet to be found while the numerical verification has been accomplished.

## 2.3. Boundary condition

The Jacobian matrix  $\mathbf{K}$  may become singular due to the presence of rigid body displacement. In order to address this singularity, displacement constraints need to be applied. In PD simulations, a displacement boundary condition is enforced by imposing constraints on the displacement or velocity field within a fictitious material layer along the boundary of a non-zero volume. As the displacement of the materials points in the fictitious layer is known, the rows and columns corresponding to the material points

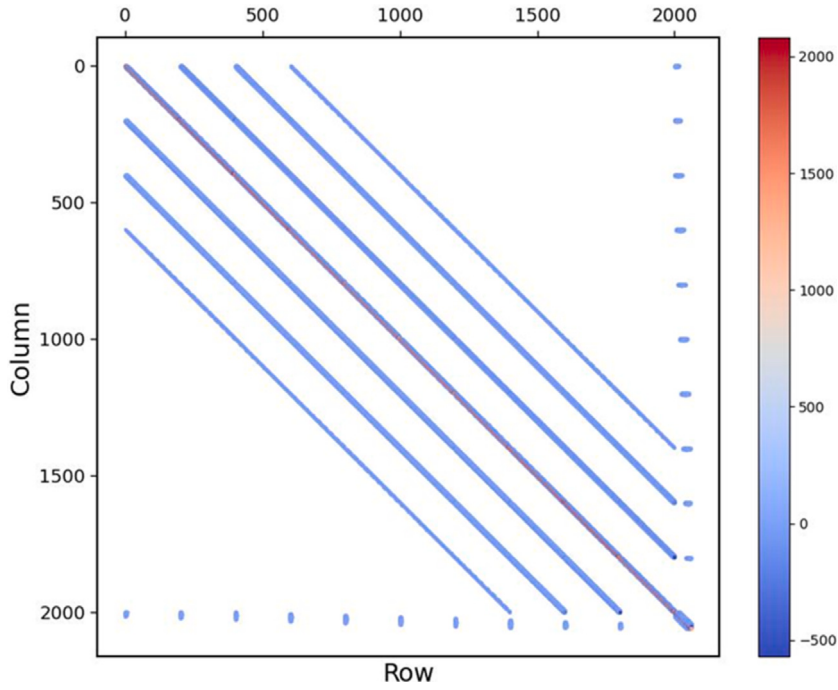


**Fig. 3.** Distribution of non-zero elements in the stiffness matrix shows the unique sparse band-like characteristics.

in the fictitious layer should be removed from the Jacobian matrix. Therefore, the row sums are no longer zero, and the singularity of  $\mathbf{K}$  is eliminated, which is shown in Fig. 4.

When applying the force boundary conditions, the external force is presented in the PD governing equation in the form of body force density vector, i.e.,  $\mathbf{b}(\mathbf{x}, t)$  in Eq. (1). In the implicit equation, it is reflected in the  $b_{ip}$  term in Eq. (11), where the subscript  $p = x, y, z$ . When force boundary conditions exist, for the PD point  $i$  where the force vector  $\mathbf{P}_i = (T_x, T_y, T_z)$  is applied, the corresponding  $b_{ix} = T_x/(s\Delta x)$ , where  $s$  is the surface area of the force boundary layer. Similarly,  $b_{iy} = T_y/(s\Delta x)$ , and  $b_{iz} = T_z/(s\Delta x)$ . For all other PD points,  $b_{ip} = 0$ .

#### 2.4. Damage evolution

A critical bond stretch is used to describe the damage evolution in the material. When the bond stretch exceeds this critical value, bonds begin to break, cracks start to form, and the interaction forces between the bonds are then set to zero. However, it is important to note that directly setting the forces to zero may adversely affect numerical convergence in the present implicit procedure. The current implicit format is based on the NR scheme, and the differentiation of forces with respect to displacement necessitates the continuity of forces. Hence, the continuous degradation function  $T_s$  is utilized to depict the deterioration of bond interaction as the bond stretch increases, which is shown below:

$$T_s = \begin{cases} 1 & (s \leq s_m) \\ \frac{1}{2} \left[ 1 - \tanh \frac{\beta(s_m + s_c - 2s)}{s_m - s_c} \right] & (s_m < s < s_c) \\ 0 & (s \geq s_c), \end{cases} \quad (12)$$

where  $s_m$  is the minimum bond stretch at which the degradation of bond interaction begins,  $s_c$  is the critical bond stretch, and  $\beta$  is a non-negative value that controls the rate of degradation [50].

The new total interaction force density vector of the particle at  $\mathbf{x}_i$ , taking into account the damage, is given by the following equation:

$$\mathbf{F}_i (\xi_{ij}, \mathbf{u}_{ij}) = \sum_{j=1}^{N_i} c_s \frac{\xi_{ij} + \eta_{ij}}{|\xi_{ij} + \eta_{ij}|} T_s \mu_{i,j} v_{i,j} V_j. \quad (13)$$

By conducting the NR procedure, the elements of new Jacobian matrix  $\mathbf{K}$  can be calculated by

$$\frac{\partial F_{ip}(\xi, \mathbf{u})}{\partial u_{jq}} = T_s P_{i,j} A_{ijpq} + P_{i,j} (T_s C_{ij} + L_{ij} B_{ij} A_{ijpq}) D_{ijpq}, \quad (14)$$

$(i, j = 1, 2, \dots, N, i \neq j; p, q = x, y, z),$

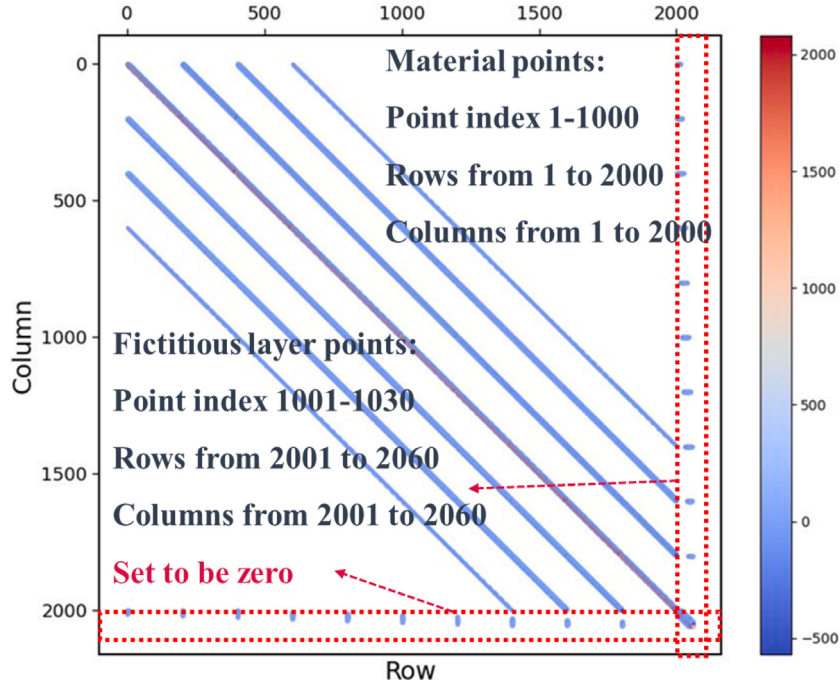


**Fig. 4.** Illustration of applying the boundary condition for a 2D bar under a transverse loading, similar to the scenario depicted in [Fig. 6](#). The boundary condition involves fixing the left side of bar.

and

$$\frac{\partial F_{ip}(\xi, \mathbf{u})}{\partial u_{iq}} = - \sum_{\mathbf{x}_j \in H_i} [T_s P_{i,j} A_{ijpq} + P_{i,j} (T_s C_{ij} + L_{ij} B_{ij} A_{ij}) D_{ijpq}], \quad (15)$$

$(i, j = 1, 2, \dots, N; \quad p, q = x, y, z),$

where  $P_{i,j} = c \mu_{i,j} v_{i,j} V_j$ ,  $A_{ijpq} = \frac{\delta_{pq}}{|\mathbf{y}_j - \mathbf{x}_i|} - \frac{\delta_{pq}}{|\mathbf{y}_j - \mathbf{y}_i|}$ ,  $B_{ij} = \frac{1}{|\mathbf{y}_j - \mathbf{x}_i| |\mathbf{y}_j - \mathbf{y}_i|}$ ,  $C_{ij} = \frac{1}{|\mathbf{y}_j - \mathbf{y}_i|^3}$  and  $D_{ijpq} = (y_{jp} - y_{ip})(y_{jq} - y_{iq})$ ,  $L_{ij} = \frac{\beta}{s_m - s_c} \left(1 - \tanh^2 \frac{\beta(s_m + s_c - 2s)}{s_m - s_c}\right)$ .

The properties of Jacobian matrix are not affected by the degradation function  $T_s$  and remain unchanged.

In summary, by introducing the degradation damage function and applying the boundary condition, the Jacobian matrix holds its sparse, symmetric, positive definite, and non-singular properties, indicating good solvability of the system.

### 3. Comparison of explicit-ADR and implicit BBPD method

The implicit scheme is often designed to reduce computational costs of PD for quasi-static problems. With the deploy of BBPD, which represents the simplest form of PD theory, and the implementation of conjugate gradient (CG) method, known as one of the simplest and most efficient iterative methods for solving linear equations, our implicit scheme is a promising method. Therefore, it would be persuasive to evaluate the efficiency of our implicit scheme by comparing to the explicit-ADR method.

For consistency, the whole-field displacement convergence is maintained for both the explicit-ADR and implicit schemes, as described below:

$$e_{\mathbf{u}} = (\|\mathbf{u}_n - \mathbf{u}_{n-1}\|_2) / \|\mathbf{u}_{n-1}\|_2, e_0 < e_0, \quad (16)$$

where  $e_{\mathbf{u}}$  is the defined relative error of whole-field displacement at the step  $n$ ,  $e_0$  is the converge criterion,  $\mathbf{u}_n$  and  $\mathbf{u}_{n-1}$  are the displacement at the steps  $(n-1)$  and  $n$ , respectively. The same material properties, geometric information, discretization length, boundary conditions, initial loading conditions, and displacement convergence criteria are used. Additionally, the degradation function with the same fracture criterion is applied to describe the bond failure in both simulations. All the calculations are conducted using Julia [57] programming within the same computational environment, utilizing a single core of the AMD EPYC 7763 64-Core Processor. Subsequently, the results of damage, displacement, and CPU time for computations are compared.

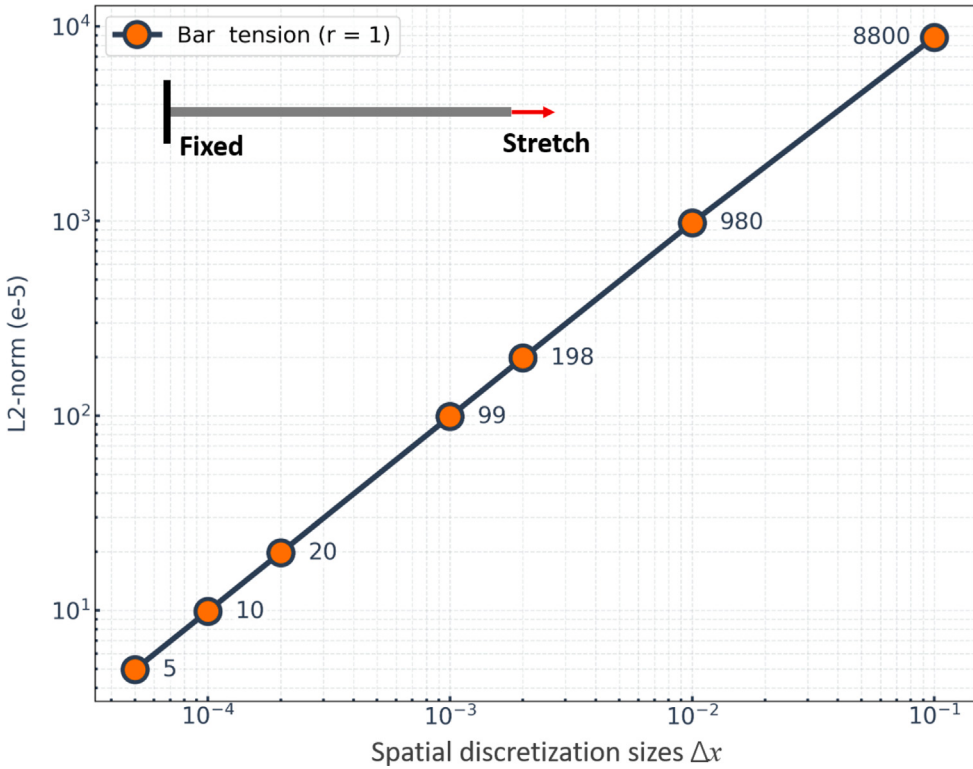


Fig. 5. Convergence of the L2-norm for displacement of the bar under tension.

### 3.1. Deformation of 1D bar under tension

The configuration comprises a 1D bar with length  $L = 1$  m, cross sectional area  $A = 10^{-6}$  m<sup>2</sup>, density  $\rho = 7850$  kg/m<sup>3</sup>, and elastic modulus  $E = 2 \times 10^{11}$  Pa. The left end ( $x = 0$ ) is fixed, while a tensile force  $F = 200$  N is applied at the right end ( $x = L$ ), as shown in Fig. 5. The analytical displacement solution is expressed as  $\mathbf{u}^a(x) = \frac{Fx}{AE}$ . Implicit simulations are conducted with spatial discretization size of  $\Delta x = \frac{1}{10}, \frac{1}{100}, \frac{1}{500}, \frac{1}{1000}, \frac{1}{5000}, \frac{1}{10000}, \frac{1}{20000}$  m, respectively. The  $L_2$ -norm error is computed to quantify numerical deviations [58], which is defined as  $\|\mathbf{u}\|_{L2} = \sqrt{\frac{\sum_j (\mathbf{u}_j - \mathbf{u}_j^a) \cdot (\mathbf{u}_j - \mathbf{u}_j^a) \Delta V_j}{\sum_j \mathbf{u}_j^a \mathbf{u}_j^a \Delta V_j}}$ . With the refinement in discretization, the numerical results converge to the theoretical solutions at a rate  $r \approx 1$ .

### 3.2. Deformation of undamaged 2D plate

The 2D plate has the initial length  $l$  of 0.5 m, and the width  $w$  of 0.05 m. It is uniformly discretized into 1030 particles using the regular grid  $100 \times 10$ , with a layer of fictitious thickness  $3\Delta x$  at the fixed boundary on the left side of the bar. The horizon size is  $3.015\Delta x$ . The material is assumed to be isotropic and linear elastic with the Young's modulus  $E$  of 200 GPa and the density of 7850 kg/m<sup>3</sup>. The boundary and loading conditions are depicted in Fig. 6. The left end of the bar is fixed, while the right end is subjected to a downward vertical loading of 125 N. The loading boundary is located on the outermost layer of the right end of the bar, with a boundary layer volume of  $10 \times 1 \times (\Delta x)^3$ . The loading is applied from the beginning as a body force density vector to the PD points within the loading boundary layer, with a magnitude of  $1 \times 10^8$  N/m<sup>3</sup>.

Both the implicit and explicit schemes adhere to the same convergence criterion as described in Eq. (16), and  $e_0$  is set to be  $1 \times 10^{-9}$ . The implicit simulation converges in only one step, while the explicit one requires approximately 20000 steps. This is because small loading increment is required to satisfy the small displacement assumption of the explicit-ADR method [9], leading to a large number of steps, whereas it is not required for the present implicit method.

No damage is allowed in this scenario. As depicted in Fig. 6, the results from the implicit simulation are identical to those obtained from the explicit simulations. But the implicit scheme is approximately 290 times faster than the explicit one.

### 3.3. Fracture of 2D plate with a hole

The 2D plate has the initial length  $l$  of 0.15 m, and the width  $w$  of 0.05 m. It is uniformly discretized into 7800 PD particles using the regular grid of  $150 \times 50$ , with two layers of fictitious thickness  $3\Delta x$  at the displacement boundary on both the left and right

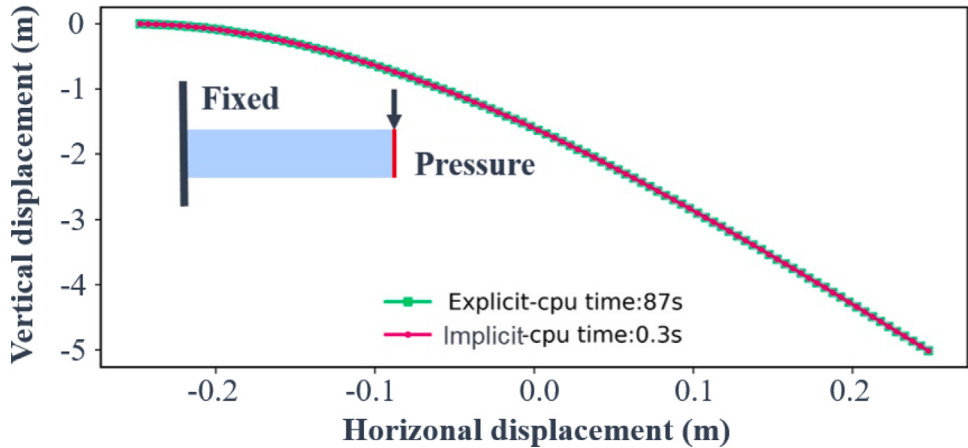


**Fig. 6.** This figure illustrates the vertical displacement distribution along the horizontal central line of a 2D bar subjected to transverse loads. The results are obtained from the explicit-ADR and implicit simulations, respectively. The loading position is marked in red.

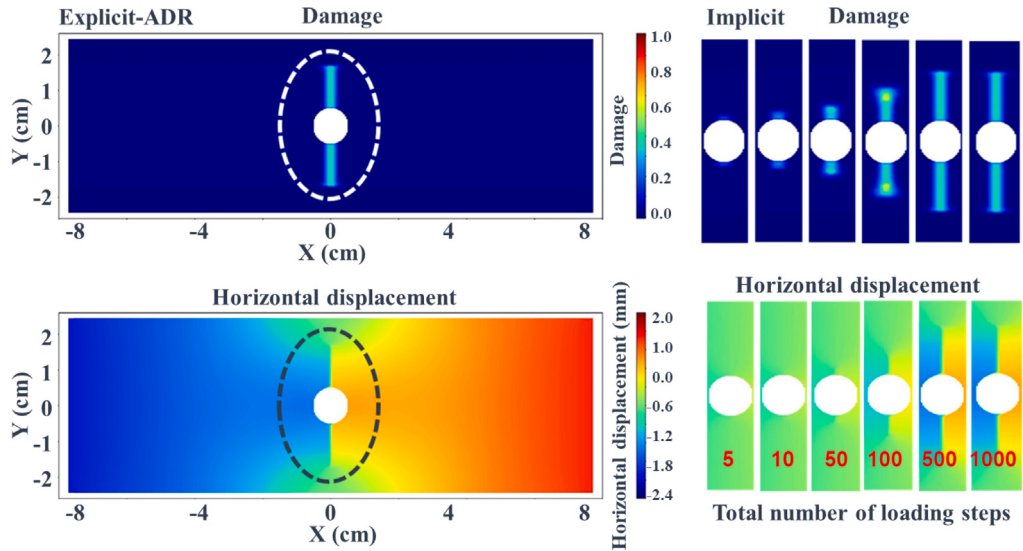


**Fig. 7.** The damage and horizontal displacement distribution of a 2D plate under horizontal tension are depicted. The left figure illustrates the results obtained from the explicit-ADR scheme, while the right figure displays the outcomes of the implicit scheme with different number of loading steps. It is noteworthy that the right figure only represents the portion enclosed within the dashed boxes of the left figure.

sides of the plate. The radius of the central hole is 0.005 m. The horizon size is  $3.015\Delta x$ . The material is assumed to be isotropic and linear elastic with the Young's modulus  $E$  of 192 GPa and the density of  $8000 \text{ kg/m}^3$ . The boundary and loading conditions are depicted in Fig. 7. The left and right ends are subjected to the outward horizontal displacement loadings with a total magnitude of 1.6 mm.

The convergence criterion remains the same as described in Section 3.1. Fracture evolution is taken into consideration, and both the implicit and explicit simulations employ the same degradation function to characterize bond damage behavior, as outlined in Eq. (12), with  $s_m = 0.033$ ,  $s_c = 0.066$ , and  $\beta = 3$ .

It is worth noting that in this example, the implicit simulation does not converge in one single step but requires multiple loading steps for convergence. For the explicit-ADR, the total displacement loading is attained by applying a small velocity at the boundary over an extended period. Note, the velocity here, as in [38], represents the displacement loading rate, which is the displacement increment in each iteration. The velocity should be small enough to avoid any dynamic effects [38]. Kilic and Madenci observed that compared to low loading rates, the results obtained using the explicit-ADR method at high loading rates exhibit significant differences and no longer adhere to the patterns observed at low loading rates. The dynamic effects originate actually from the assumption of small displacements in deriving the ADR formulation. If the loading rate is large, this fundamental assumption of the ADR method is violated, leading to incorrect results. In our case, the velocity magnitude is  $1.6 \times 10^{-7} \text{ m/iteration}$  and lasts for 10,000 loading steps.

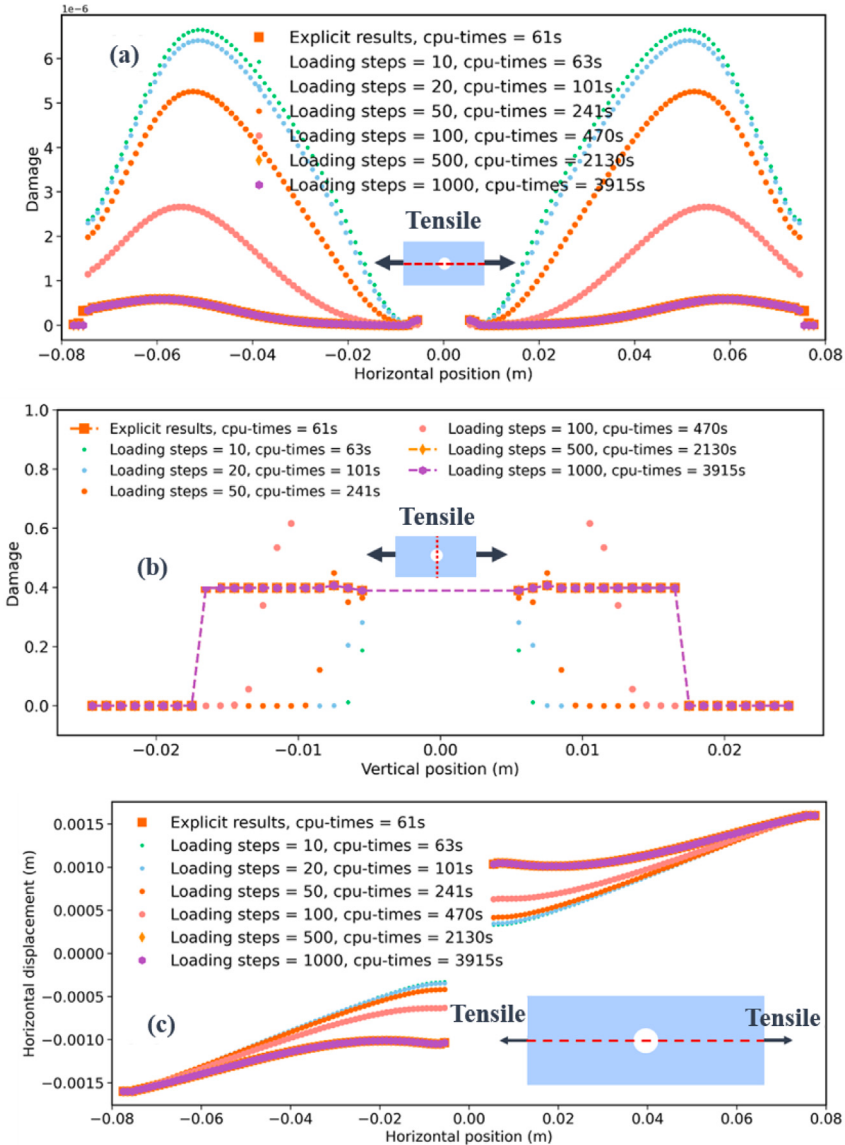


**Fig. 8.** This figure illustrates the distribution of damage and horizontal displacement along the specific lines, which are marked as the dashed red lines in each sub-figure. Different colors and markers indicate the change in number of loading steps.

Here, we can observe from Fig. 7 that the results obtained from the implicit schemes vary significantly with the number of loading steps. The results between the explicit and implicit simulations are only consistent when the number of loading steps is large enough in the implicit process, e.g., 500 and 1000. To visually observe the differences in the simulation results more intuitively, the damage distribution on the horizontal and vertical central lines are shown in Fig. 8.

It is evident that both damage and displacement vary significantly with the number of loading steps. Moreover, the results obtained from the implicit simulation converge to those from the explicit simulation as the number of loading steps increases.

As this case involves fracture propagation, the computational costs of the implicit scheme are at least 30 times larger than those of the explicit one. This is attributed to the requirement for a large number of loading steps to ensure computational accuracy.

### 3.4. Analysis of the implicit scheme for fracture evolution

Fig. 8 illustrates that the number of loading steps is crucial for computing fracture propagation. In essence, a smaller total number of steps leads to larger loading increments for each step, influencing the bond failure process and consequently leading to different

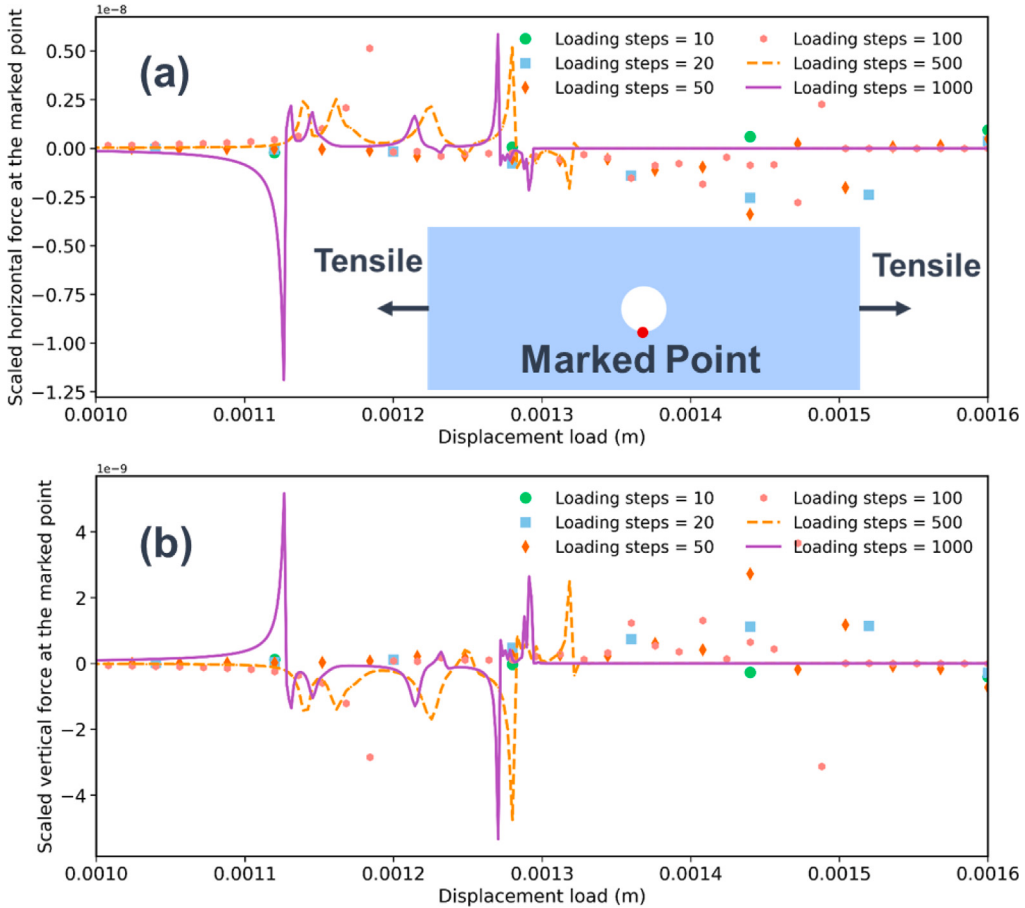


**Fig. 9.** Figures (a) and (b) illustrate the variation of horizontal and vertical forces at the marked points as the number of loading steps changes, while the total displacement remains constant. The local force density is obtained during the implicit simulation procedure. Different colors and markers indicate changes in the number of loading steps. The scaling factor is denoted as  $Q$  ( $Q = \Delta x^3$ ). The total displacements remain constant at 1.6 mm, while the number of loading steps vary, ranging from 10 to 2000.

simulations results. Previous studies have suggested that controlling the maximum number of failed bonds at each step is essential for accurate implicit simulations [52]. In other words, the smaller the loading increment, the less bond failure occurs at each step, and the more accurate the implicit scheme is for fracture problems. Increasing the number of loading steps to reduce the amplitude of the loading increment at each step is one of the most effective methods for controlling the maximum number of failed bonds at each step, even though it may significantly decrease the efficiency of the implicit scheme. It can be concluded that the implicit scheme is not an efficient choice to simulate fracture problems compared to the explicit-ADR method.

When a bond fails, the local forces applied to a PD node experience significant variations in terms of both magnitude and direction, regardless of the type of bond failure, i.e., whether it occurs as a sudden release or through a degradation model. The differentiation or finite difference in the forces acting on each PD point constitutes the primary element of the Jacobian matrix as depicted in Eq. (6). If the local forces exhibit pronounced fluctuations, the elements of the Jacobian matrix are inevitably affected and undergo significant variations. In the implicit format, the variations of PD forces are reflected in the elements of the Jacobian matrix.

To address the significant variations in local forces during fracturing process, it is necessary to use sufficiently small loading increments, resulting in a large yet essential number of loading steps. Fig. 9 presents the scaled forces of the first-damaged PD point (marked point) during the loading process of the case discussed in Section 3.3.

It is evident that a small number of loading steps smooth out the fluctuations in the local forces and significantly under-predict the variation of local forces once the fractures occur, which fails to describe the interaction forces between the PD points, leading to inaccurate results. Only with a sufficiently large total loading steps, the variation of local PD forces during fracturing process can be accurately described, making the number of loading steps critical for the implicit simulation to calculate fracture evolution.

It can be concluded that the implicit scheme is more suitable and effective compared to the explicit-ADR scheme for quasi-static problems without fractures. This is due to its very fast convergence speed and very few loading steps. However, when fracture

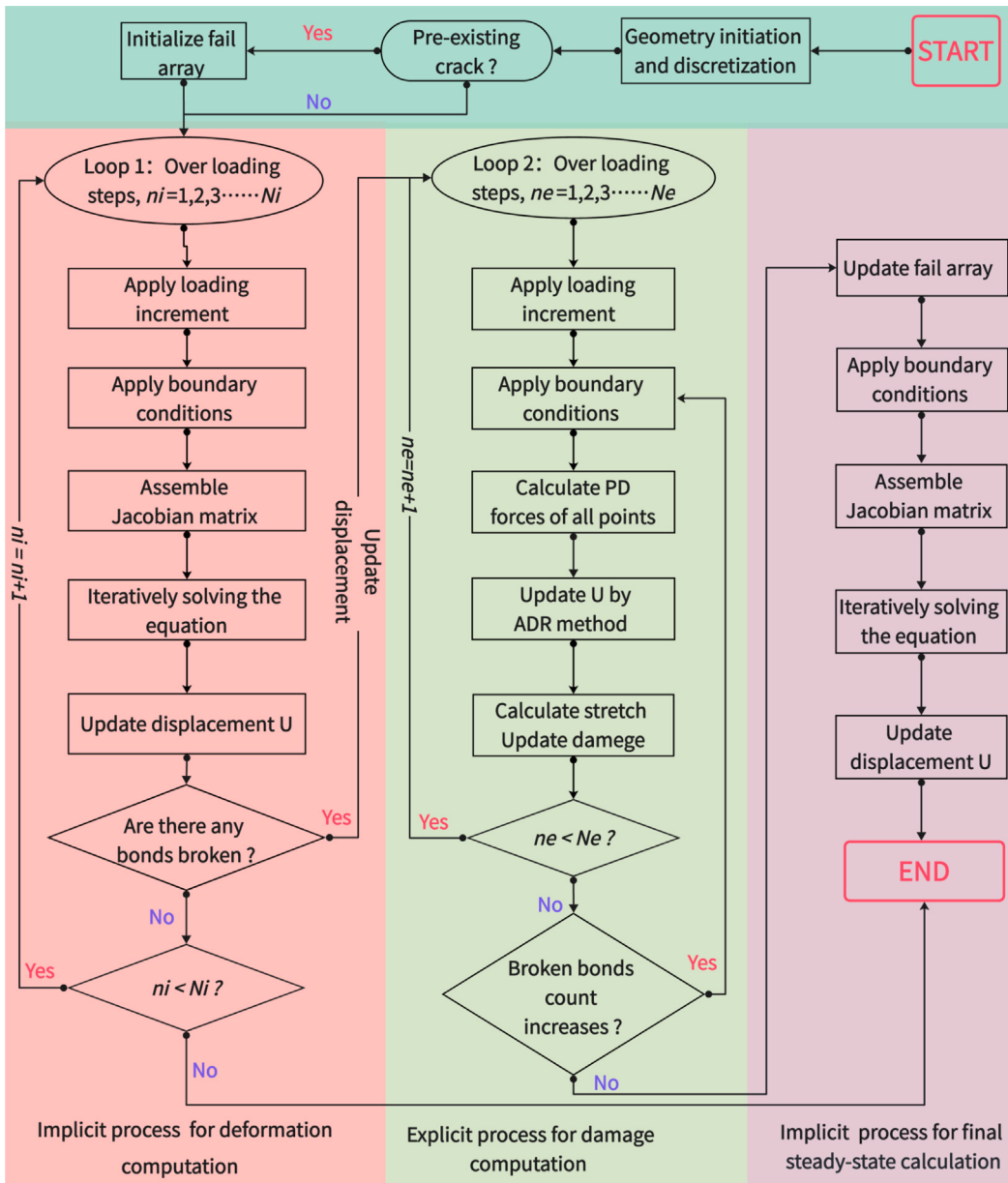


**Fig. 10.** The adaptive process flowchart is depicted here.  $N_i$  and  $N_e$  are the number of loading steps of the implicit and explicit processes, respectively, to reach the total displacement load.

evolution is considered, the implicit scheme may require significantly more computational time than the explicit-ADR scheme due to the need for a sufficiently large number of loading steps to ensure accuracy.

To utilize the efficiency of the implicit scheme for quasi-static problems without fracture and mitigate its disadvantages in simulating fracture formation problems, we propose an adaptive strategy for quasi-static fracture formation problems, which will be presented in Section 4.

#### 4. Adaptive strategy for quasi-static fracture problems

The proposed adaptive scheme is illustrated in Fig. 10. The entire process for solving quasi-static fracture problems is divided into three steps. The first step involves the implicit process for deformation computation, extending from the onset of deformation

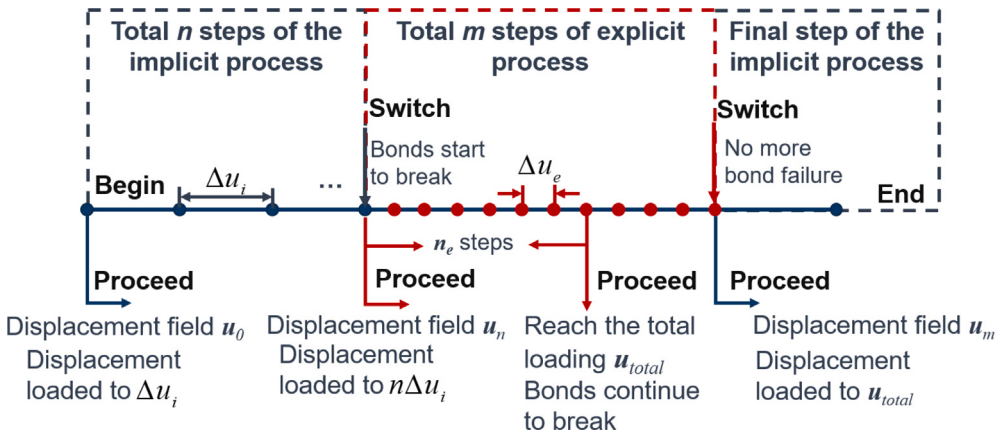


**Fig. 11.** The schematic diagram of displacement loading throughout the entire computation process, where  $\Delta u_i, \Delta u_e$  denote the displacement loading increments for the implicit and explicit simulations, respectively, and  $u_{total}$  is the total displacement loading. The initial implicit process consists of  $n$  steps, while the explicit process consists of  $m$  steps, with  $N_e$  steps to reach the total displacement load. The relationship between the displacement increments and the total displacement is  $u_{total} = n \times \Delta u_i + N_e \times \Delta u_e$ .

to crack initiation. The second step comprises the explicit-ADR process for damage computation, continuing from the implicit step with inherited displacement and loading information, which proceeds until bond failure ceases. The final step switches back to the implicit process until completion.

When the tensile stretch of any bond exceeds a certain threshold, denoted as  $s_m$ , the implicit process terminates and switches to the explicit ADR process. Once the displacement reaches a final state, where no more bonds fail over an extended period, the explicit ADR process terminates, and the final implicit process resumes. Fig. 11 illustrates the displacement increments for both the implicit and explicit schemes.

It is worth noting that  $n$  in Fig. 11 represents the actual number of computational steps executed in the initial implicit simulation of a general case, while  $N_i$  in Fig. 10 is the number of steps set before calculation to generate an implicit loading increment  $\Delta u_i$ ,  $\Delta u_i = u_{total}/N_i$ . In all the simulations,  $n$  is not larger than  $N_i$ .

## 5. Numerical validation

We apply the present adaptive and explicit-ADR method to solve four different quasi-static problems. All the calculations are conducted using Julia programming utilizing a single core of the AMD EPYC 7763 64-Core Processor. The results and the processing times are compared using the same converge criterion.

### 5.1. Deformation of undamaged 3D bar under a transverse loading

In this benchmark case [9], the 3D bar has the initial length  $l$  of 1 m, the width  $w$  of 0.1 m, and the height  $h$  of 0.1 m. The domain is uniformly discretized into 10,300 particles using the regular grid of  $100 \times 10 \times 10$ , with an additional layer of fictitious thickness  $3\Delta x$  at the fixed boundary on the left side of the bar. The horizon size is  $3.015\Delta x$ . The material is assumed to be isotropic and linear elastic with the Young's modulus  $E$  of 200 GPa and the density  $\rho$  of 7850 kg/m<sup>3</sup>. The boundary and loading conditions are depicted in Fig. 12(b). The left end of the bar is fixed, while the right end is subjected to a downward vertical loading of 5000 N. The loading boundary is located on the outermost layer of the right end of the bar, with a boundary layer volume of  $10 \times 10 \times (\Delta x)^3$ . The loading is applied from the beginning as a body force density vector to the PD points within the loading boundary layer, with a value of  $5 \times 10^7$  N/m<sup>3</sup>.

In this case, both the adaptive and explicit-ADR methods directly utilize the total pressure loading as the boundary condition and adhere to the same convergence criterion, as described in Eq. (16), where  $e_0$  is set to be  $1 \times 10^{-9}$ . The adaptive method achieves convergence in just one step, while the explicit one requires approximately 20,000 steps.

We found that the results of the present adaptive method are consistent with those of the explicit scheme reported in the literature [9], with an acceleration ratio of approximately 141.7.

### 5.2. Damage evolution of a 2D square plate with a central hole under tensile loadings

This case is similar to the benchmark example of the citation [50], the 2D square plate has the initial length  $l$  of 0.05 m. It is uniformly discretized into 2900 particles using the regular grid of  $50 \times 50$ , with two additional layers of fictitious thickness  $3\Delta x$  at the displacement boundaries on both the top and bottom sides of the plate. The radius of the central hole is 0.005 m. The horizon size is  $3.015\Delta x$ . The material is assumed to be isotropic and linear elastic with the Young's modulus  $E$  of 192 GPa and the density

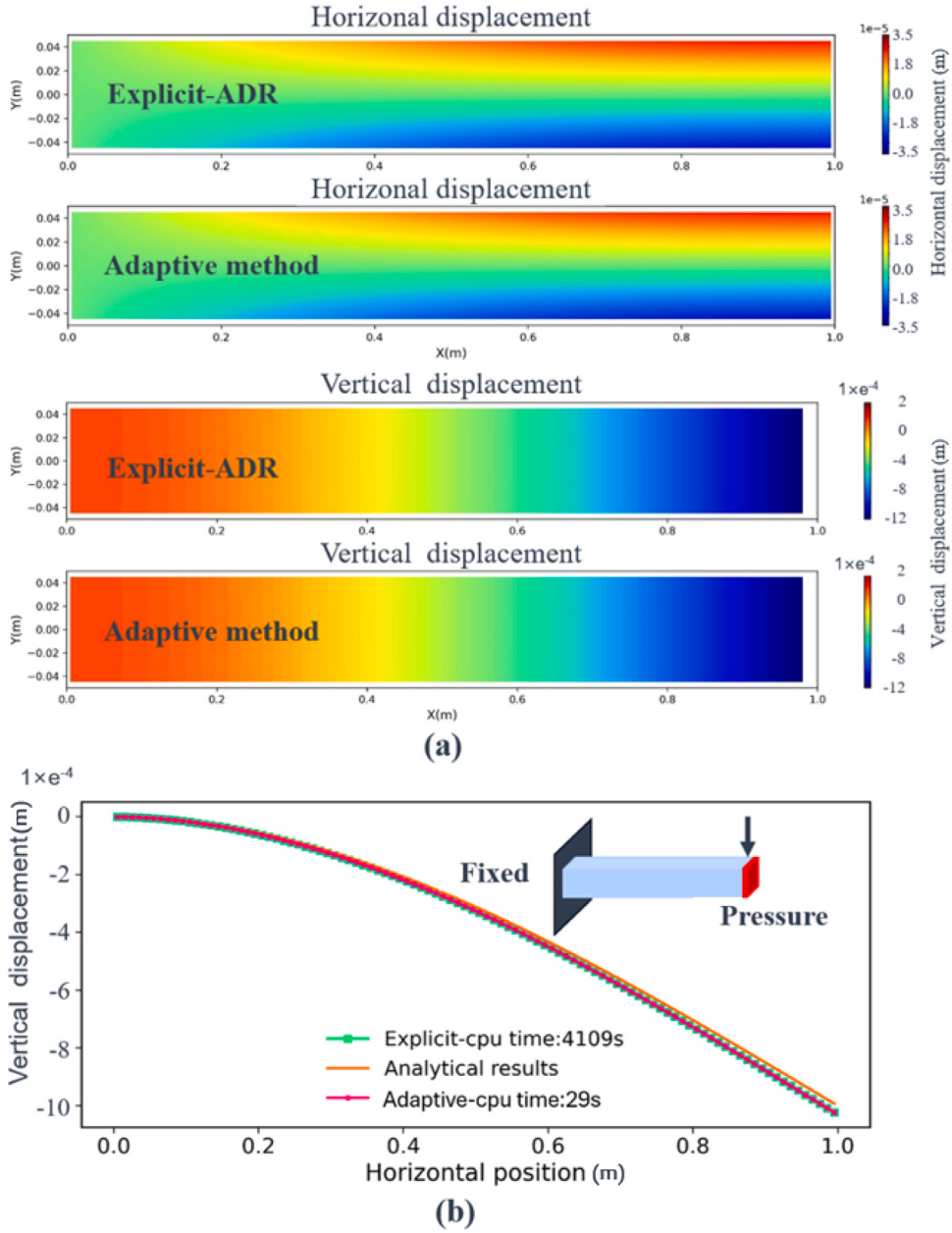


**Fig. 12.** Figure (a) shows the contour diagrams of horizontal and vertical displacement obtained by the explicit-ADR and adaptive methods. Figure (b) shows the vertical displacement distribution along the horizontal central line of the bar, and the schematic diagram of geometry, boundary and loading. The loading position is marked in red.

$\rho$  of  $8000 \text{ kg/m}^3$ . The bond failure criterion is based on the degradation form as outlined in Eq. (12), with  $s_m = 0.015$ ,  $s_c = 0.02$ , and  $\beta = 3$ . The boundary and loading conditions are depicted in Fig. 13(b). The upper and lower ends of the plate are subjected to the outward vertical displacement loadings with a magnitude of 0.275 mm.

In this case, the total displacement loading is applied through both implicit and explicit loading processes in the adaptive method. The maximum number of steps for the implicit and explicit loading processes is set to be 3 and 180, respectively. This implies that the loading rate for deformation computation is  $2.75 \times 10^{-4}/3 \text{ m/iteration}$ , while the loading rate for damage evolution computation is  $(1 - n/3) \times 2.75 \times 10^{-4}/180 \text{ m/iteration}$ , where  $n$  is the step at which damage initiation occurs, as depicted in Fig. 11. As for the explicit-ADR scheme, the loading rate is set to be  $2.75 \times 10^{-7} \text{ m/iteration}$ . In addition, both the adaptive and explicit methods use the same convergence criterion, as described in Eq. (16), where  $e_0$  is set to be  $1 \times 10^{-9}$ .

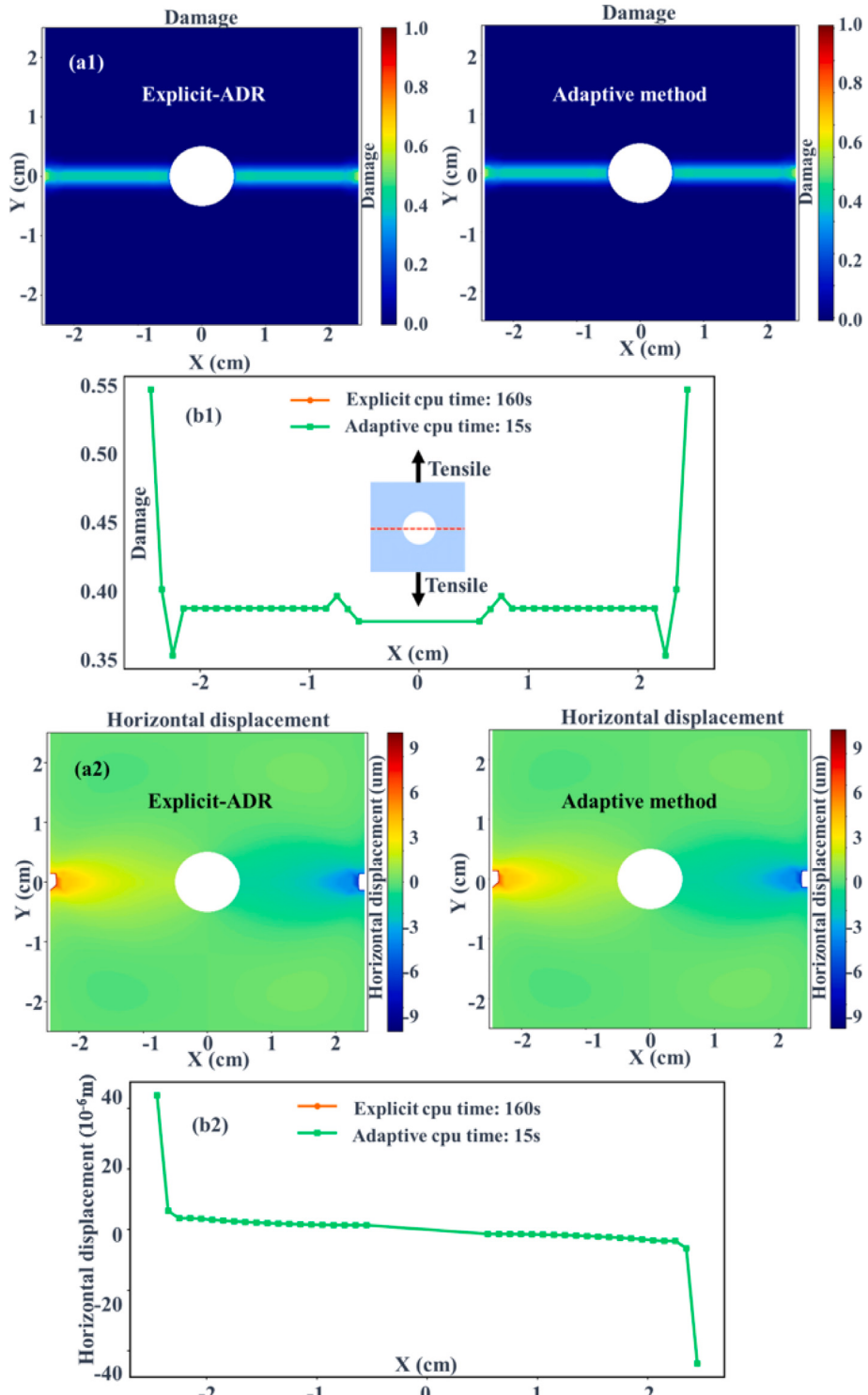


**Fig. 13.** The schematic diagram of geometry, boundary and loading is shown in (b1). (a1)–(a3) display the contour diagrams illustrating the distribution of damage, horizontal displacement, and vertical displacement. (b1)–(b3) depict the distribution of damage, horizontal displacement, and vertical displacement along the horizontal central line of the bar, which corresponds to the central axis at  $y = 0$ , as denoted by the red dashed line in (a1).

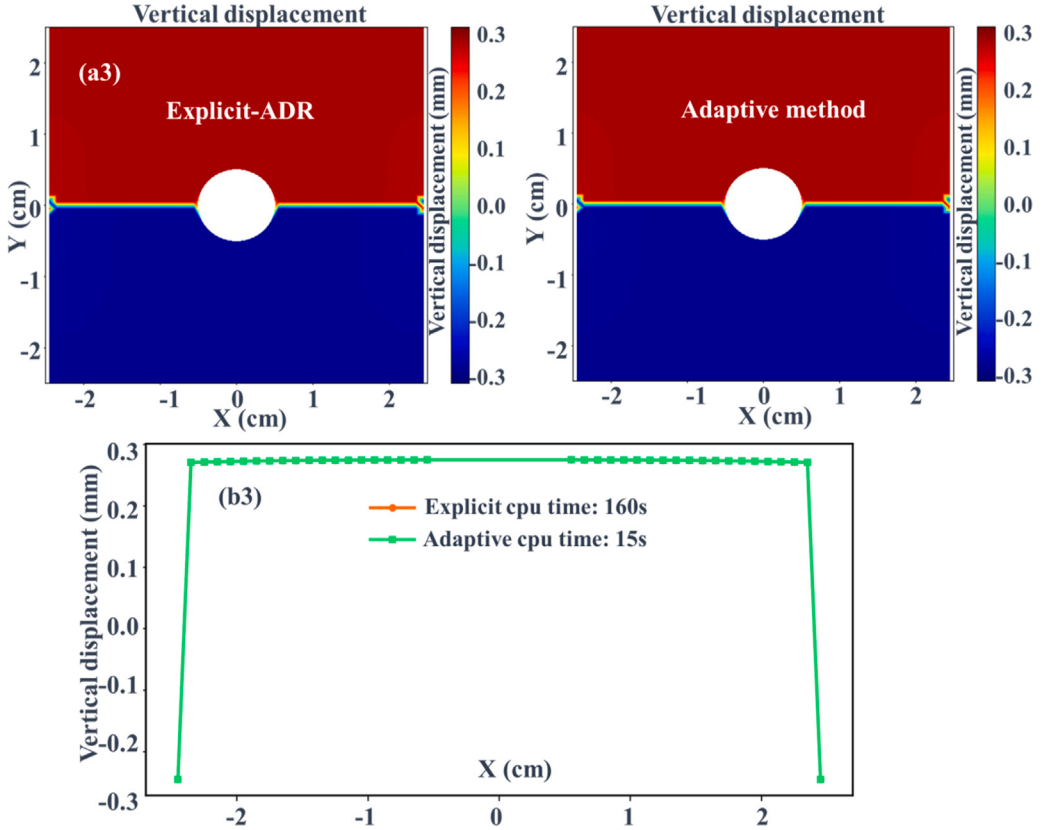


Fig. 13. (continued).

As shown in Fig. 12(b1–b3), the red and green lines match each other perfectly, indicating that the adaptive computation results are in excellent agreement with those obtained from the explicit-ADR simulation, with an acceleration ratio of 10.7.

### 5.3. Damage evolution of a 2D plate subjected to three point bending

In this case, the 2D rectangular plate has the initial length  $l$  of 0.24 m, and the width  $w$  of 0.06 m. It is uniformly discretized into 10,048 PD particles using the regular grid of  $200 \times 50$ , with three additional areas of fictitious thickness  $3\Delta x$ , and the span  $4\Delta x$  at the displacement boundary on the three point for loading. The pre-existing notch is located at the center of the lower end, oriented vertically, with the length of  $0.3w$  and the span of  $2\Delta x$ . The horizon size is  $3.0154\Delta x$ . The material is assumed to be isotropic and linear elastic with the Young's modulus  $E$  of 200 GPa and the density  $\rho$  of  $8000 \text{ kg/m}^3$ . The bond failure criterion is based on the degradation form as described in Eq. (12), with  $s_m = 0.016$ ,  $s_c = 0.02$ , and  $\beta = 3$ . The boundary and loading conditions are depicted in Fig. 14 (b1).

As for the three point bending test, two points at the lower end are constrained from the vertical movement, each with a horizontal distance of 0.105 m from the center. Additionally, one last point located at the center of the upper end is subjected to the downward vertical displacement loading with a magnitude of 4 mm.

Here, the maximum number of steps for the implicit and explicit loading processes is set to be 5 and 1000 for the adaptive method, respectively. This implies that the loading rate for deformation computation is  $4 \times 10^{-3}/5$  m/iteration, and for damage evolution computation is  $(1 - n/5) \times 4 \times 10^{-3}/1000$  m/iteration, where  $n$  is the step at which damage initiation occurs, as depicted in Fig. 11. As for the explicit-ADR scheme, the loading rate is set to be  $1 \times 10^{-7}$  m/iteration. In addition, both the adaptive and explicit methods use the same convergence criterion, as described in Eq. (16), where  $e_0$  is set to be  $1 \times 10^{-9}$ .

The results of the current adaptive method are in excellent agreement with those obtained by the explicit scheme, exhibiting an acceleration ratio of around 6.4.

### 5.4. Damage evolution of a 2D plate with multiple holes under a concentrated tensile loading

In this case, the 2D plate has the initial length  $l$  of 0.065 m, the width  $w$  of 0.12 m, as described in [59]. It is uniformly discretized into about 7800 particles using the regular grid of  $65 \times 120$ . There are four holes in the plate. The radius of the upper left and

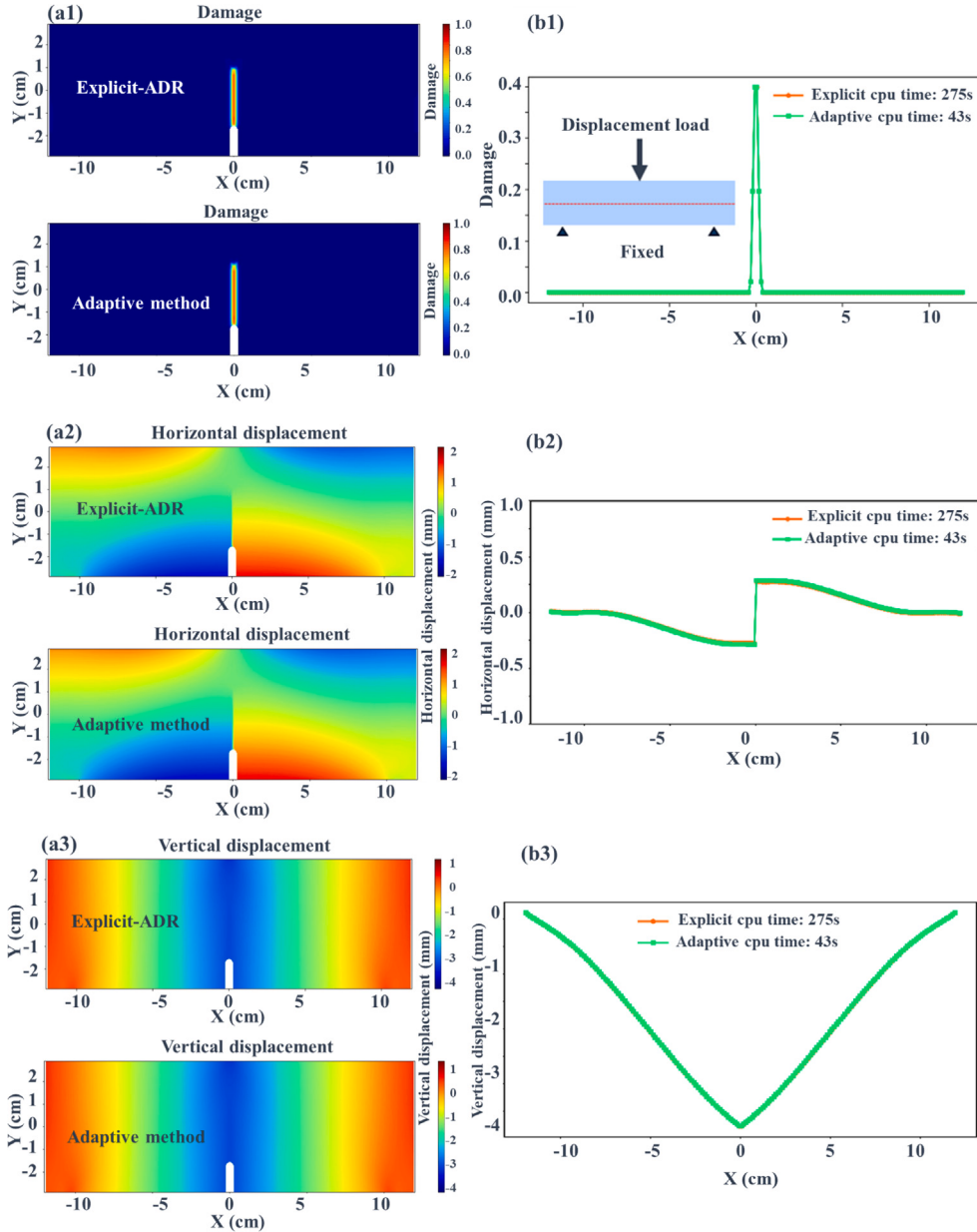


**Fig. 14.** The schematic diagram of geometry, boundary and loading is shown in (b1). (a1)–(a3) display the contour diagrams for the distribution of damage, horizontal displacement, and vertical displacement, respectively. (b1)–(b3) show the damage, horizontal displacement, and vertical displacement along the horizontal central line of the plate, respectively.

lower left holes for loading is 6.5 mm, while the radius of the smaller hole in the middle is 6 mm, and the radius of the larger one is 10 mm. The geometric layout is shown in Fig. 15.

In all the simulations, the linear isotropic elastic model is applied, with the Young's modulus  $E$  of 200 GPa and the density  $\rho$  of 8000 kg/m<sup>3</sup>. The bond failure criterion follows Eq. (12), with  $s_m = 0.016$ ,  $s_c = 0.02$ , and  $\beta = 3$ . The boundary and loading conditions are shown in Fig. 17(a1), where the holes on the left side experience the outward vertical displacement loadings of  $8.0 \times 10^{-4}$ m.

Note that, considering the elimination of dependence on the regular distribution of PD points during crack propagation [60], we first examine the influence of the horizontal radius on the calculation results, as shown in Fig. 16. The ADR method is applied with the horizon radius varying from  $3.015\Delta x$  to  $8.015\Delta x$ .

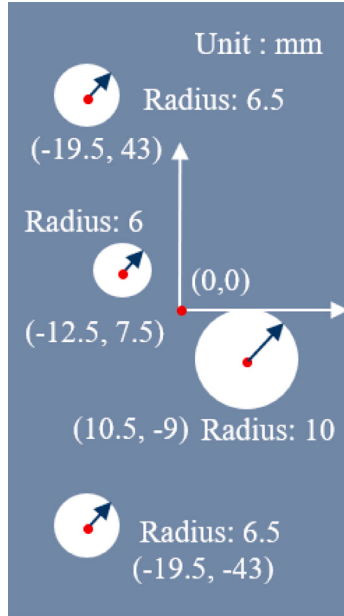


Fig. 15. The detailed geometric layout, where the values in parentheses represent the coordinates of the hole centers.

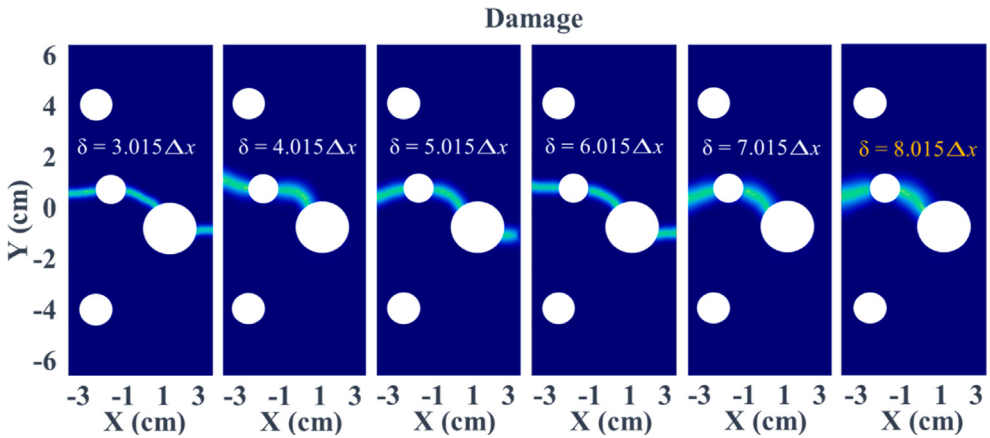


Fig. 16. The crack paths of the perforated plate under slow tension. The paths change with different horizon size.

It can be observed that as the radius increases, the crack morphology becomes consistent, indicating that when the radius is around  $8.015\Delta x$ , the grid dependence of crack propagation disappears. A horizon radius of  $8.015\Delta x$  is selected for the subsequent calculations of fracture evolution. For the adaptive method, a horizon size of  $3.015\Delta x$  is used throughout the material during the implicit simulation of the deformation stage.

Here, the maximum number of steps for the implicit and explicit loading processes is set to be 5 and 1500 for the adaptive method, respectively. This implies that the loading rate for deformation computation is  $8.0 \times 10^{-4}/5$  m/iteration, and for damage evolution computation is  $(1-n/5) \times 8.0 \times 10^{-4}/1500$  m/iteration, respectively, where  $n$  is the step at which damage initiation occurs, as depicted in Fig. 11. As for the explicit-ADR scheme, the loading rate is set to be  $1 \times 10^{-8}$  m/iteration. Both the adaptive and explicit methods use the same convergence criterion with  $e_0 = 1 \times 10^{-9}$  as described in Eq. (16).

The results of the current adaptive method are in excellent agreement with those obtained by the explicit scheme, exhibiting an acceleration ratio of around 46.4.

In summary, the table below lists the computational time consumed for the above four test cases. All the calculations were conducted, using Julia programming, on a single core of the AMD EPYC 7763 64-Core Processor (see Table 1).

It can be observed from the above simulations that the present adaptive method can efficiently solve quasi-static fracture problems, akin to the explicit-ADR scheme, which reduces computational costs significantly compared to the explicit scheme. We observe that the acceleration ratio  $r_a$  of the adaptive method in comparison with the explicit-ADR scheme for the above four cases

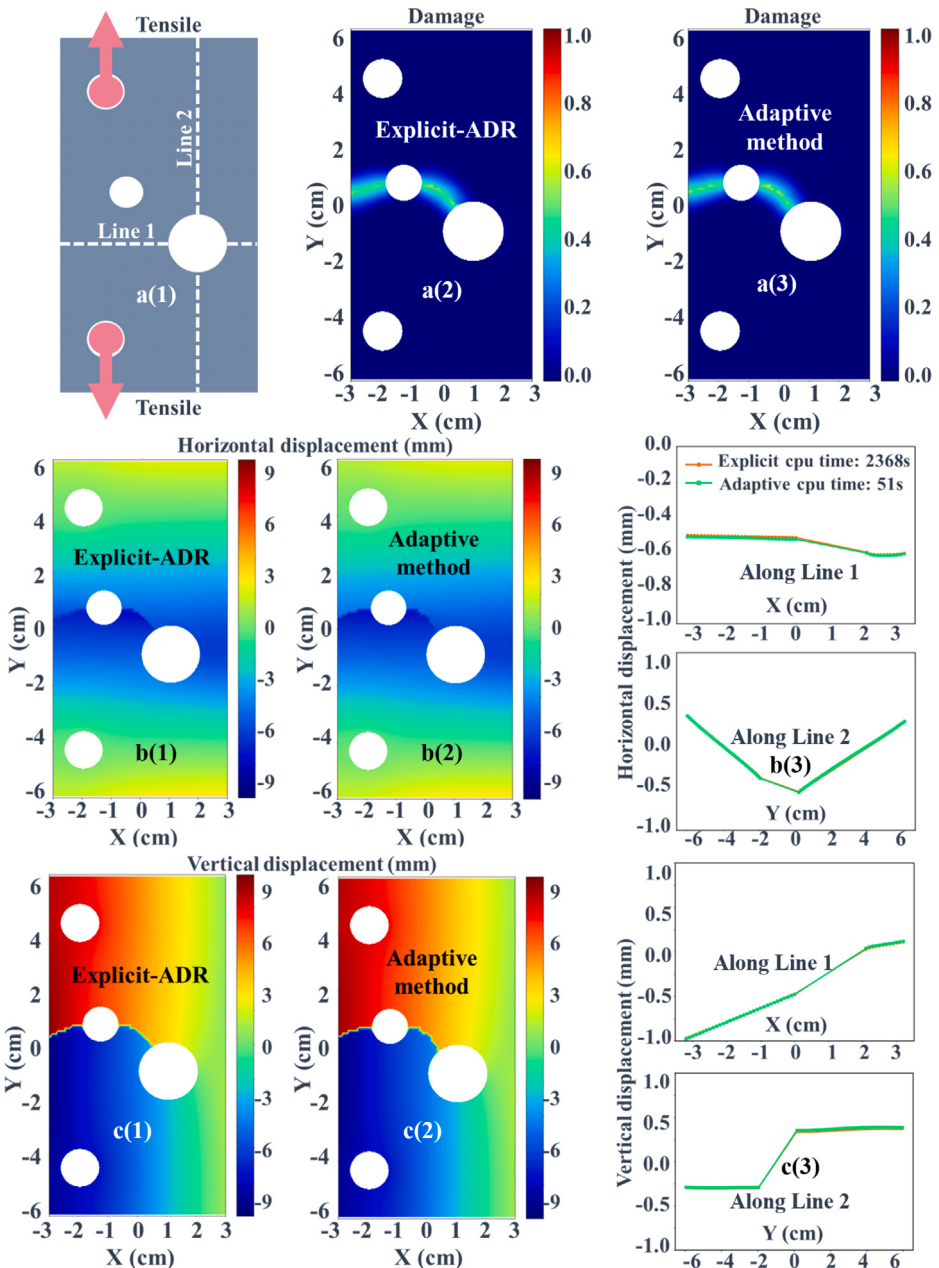


**Fig. 17.** Comparison of the explicit and adaptive methods. (a2)–(a3) show the damage distribution, (b1)–(b2) display the horizontal displacement, and (c1)–(c2) present the vertical displacement. (b3) and (c3) illustrate the horizontal and vertical displacement along Line 1 and Line 2, which are marked in (a1) by the white dashed lines.

**Table 1**  
Summary of computational time.

Case Number	explicit-ADR method (s)	Adaptive method (s)	Acceleration ratio of adaptive to explicit-ADR method
1	4109	29	141.7
2	160	15	10.7
3	275	43	6.4
4	2368	51	46.4

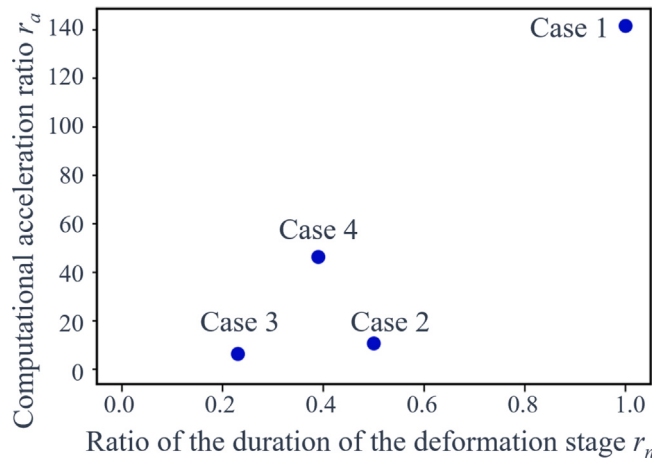


**Fig. 18.** The relationship between  $r_n$  and  $r_a$  for the four test cases.

ranging from 6.4 to 141.7. In the entire simulation process of the 4 cases, including deformation and fracture propagation, we calculate the ratio  $r_n$  of the number of steps from the beginning to fracture initiation to the total number of steps required for convergence to the specified precision, and reveal the relationship between acceleration ratios  $r_a$  and  $r_n$  as shown in Fig. 18.

It is evident that  $r_n$  plays a significant role in the acceleration performance of the adaptive method: the larger  $r_n$ , the greater proportion of the deformation process in the entire process, and the better acceleration ratio due to more significant contribution of the implicit scheme. The result of Case 4 is unexpected, as its acceleration ratio  $r_a$  is much larger than anticipated. The reason for this discrepancy is that, in Case 4, the acceleration effect stems not only from the greater proportion of the deformation process but also from the much smaller horizon size of  $3.0154\Delta x$  for the deformation stage of the adaptive method compared to  $8.0154\Delta x$  for the explicit scheme. Furthermore, due to the larger horizon size, which would result in a significant computational burden, the acceleration effect of the latter is more pronounced.

## 6. Concluding remarks

In this study, we have developed an efficient implicit BBPD model for solving quasi-static problems based on the full nonlinear equilibrium equation with a degradation bond failure function. We compared the computational efficiency of the explicit-ADR method and the newly-developed implicit method. Based on this, we proposed an adaptive explicit-implicit PD method to enhance computational efficiency for solving quasi-static problems. Three main conclusions drawn from this work:

(1) The Jacobian matrix based on the full nonlinear BBPD, derived from the NR procedure, exhibits typical properties such as sparsity, symmetry, and non-singularity, indicating good solvability.

(2) Regarding the computational efficiency of solving quasi-static problems using PD, the present implicit method performs well in computing damage-free deformations but struggles with damage evolution. This is because a sufficiently large number of loading steps are required for the implicit simulations to accurately compute damage evolution.

(3) Compared to the ADR and implicit methods, the explicit-implicit adaptive method presented in this work effectively utilizes the strengths of both methods, providing a more efficient solution for quasi-static fracture problems. Specifically, it outperforms the ADR method in the deformation stage and is more efficient than the implicit method in handling crack initiation and propagation. The accuracy and efficiency of our adaptive method are examined in the four test cases, revealing that the greater the proportion of the deformation process in the entire process, the more pronounced computational acceleration of the adaptive method.

As the current adaptive algorithm is demonstrated using BBPD, it is, at present, only applicable to linear elastic materials. Three key points are worthwhile for in-depth research in the future.

(1) No bonds fail during deformation, but the implicit simulation needs to calculate bond stretch for all the PD points at each step to decide whether to switch to the explicit scheme, which leads to substantial computational burden. The switching criteria may therefore be refined to avoid calculating bond stretch during the deformation stage, thus further reducing computational costs.

(2) The conjugate gradient method is used to solve the equations. Multiple numerical techniques, including preconditioning, may be exploited to expedite computations for large linear systems and further optimize the adaptive method.

(3) To extend the present explicit-implicit adaptive scheme to SBPD for more complex constitutive models, which is, in principle, straightforward.

## CRediT authorship contribution statement

**Shiwei Hu:** Writing – review & editing, Writing – original draft, Visualization, Validation, Software, Methodology, Investigation, Formal analysis, Data curation. **Tianbai Xiao:** Writing – review & editing, Supervision, Software, Project administration, Conceptualization. **Mingshuo Han:** Validation, Investigation. **Zuoxu Li:** Investigation, Formal analysis. **Erkan Oterkus:** Writing – review & editing, Methodology. **Selda Oterkus:** Writing – review & editing, Methodology. **Yonghao Zhang:** Writing – review & editing, Supervision, Resources, Project administration, Funding acquisition, Conceptualization.

## Declaration of competing interest

The authors declare that they have no known competing financial interests or personal relationships that could have appeared to influence the work reported in this paper.

## Acknowledgments

The authors acknowledge the financial support of the National Science Foundation of China (No. 12302381) and the computing resources provided by Hefei Advanced Computing Center.

## Data availability

Data will be made available on request.

## References

- [1] Silling SA. Reformulation of elasticity theory for discontinuities and long-range forces. *J Mech Phys Solids* 2000;48(1):175–209. [http://dx.doi.org/10.1016/S0022-5096\(99\)00029-0](http://dx.doi.org/10.1016/S0022-5096(99)00029-0).
- [2] Silling SA, Askari E. Peridynamic modeling of impact damage. In: ASME pressure vessels and piping conference, vol. 46849. 2004, p. 197–205.
- [3] Bobaru F, Silling SA, Jiang H. Peridynamic fracture and damage modeling of membranes and nanofiber networks. Tech. rep, Sandia National Lab (SNL-NM), Albuquerque, NM (United States); 2004.
- [4] Silling SA, Askari E. A meshfree method based on the peridynamic model of solid mechanics. *Comput Struct* 2005;83(17–18):1526–35. <http://dx.doi.org/10.1016/j.compstruc.2004.11.026>.
- [5] Demmie PN, Silling SA. An approach to modeling extreme loading of structures using peridynamics. *J Mech Mater Struct* 2007;2(10):1921–45. <http://dx.doi.org/10.2140/jomms.2007.2.1921>.
- [6] Gerstle W, Sau N, Silling S. Peridynamic modeling of concrete structures. *Nucl Eng Des* 2007;237(12–13):1250–8. <http://dx.doi.org/10.1016/j.nucengdes.2006.10.002>.
- [7] Silling SA, Epton M, Weckner O, Xu J, Askari E. Peridynamic states and constitutive modeling. *J Elasticity* 2007;88(2):151–84. <http://dx.doi.org/10.1007/s10659-007-9125-1>.
- [8] Silling S, Lehoucq R. Peridynamic theory of solid mechanics. In: Aref H, van der Giessen E, editors. Advances in applied mechanics. Advances in applied mechanics, vol. 44, Elsevier; 2010, p. 73–168. [http://dx.doi.org/10.1016/S0065-2156\(10\)44002-8](http://dx.doi.org/10.1016/S0065-2156(10)44002-8).
- [9] Madenci E, Oterkus E. *Peridynamic theory and its applications*. Springer New York; 2014.
- [10] Tong Q, Li S. Multiscale coupling of molecular dynamics and peridynamics. *J Mech Phys Solids* 2016;95:169–87. <http://dx.doi.org/10.1016/j.jmps.2016.05.032>.
- [11] Javili A, Morasata R, Oterkus E, Oterkus S. Peridynamics review. *Math Mech Solids* 2018;24(11):3714–39. <http://dx.doi.org/10.1177/1081286518803411>.
- [12] Pirzadeh A, Dalla Barba F, Bobaru F, Sanavia L, Zaccariotto M, Galvanetto U. Elastoplastic peridynamic formulation for materials with isotropic and kinematic hardening. *Eng Comput* 2024;40(4):2063–82. <http://dx.doi.org/10.1007/s00366-024-01943-x>.
- [13] Han F, Lubineau G, Azdoud Y. Adaptive coupling between damage mechanics and peridynamics: A route for objective simulation of material degradation up to complete failure. *J Mech Phys Solids* 2016;94:453–72. <http://dx.doi.org/10.1016/j.jmps.2016.05.017>.
- [14] Torabi AR, Majidi HR, Amani H, Akbaroost J. Implementation of XFEM for fracture prediction of VO-notched brittle specimens. *Eur J Mech A Solids* 2020;81:103970. <http://dx.doi.org/10.1016/j.euromechsol.2020.103970>.
- [15] Zhou X, Chen J. Extended finite element simulation of step-path brittle failure in rock slopes with non-persistent en-echelon joints. *Eng Geol* 2019;250:65–88. <http://dx.doi.org/10.1016/j.enggeo.2019.01.012>.
- [16] Moés N, Dolbow J, Belytschko T. A finite element method for crack growth without remeshing. *Internat J Numer Methods Engrg* 1999;46(1):131–50. [http://dx.doi.org/10.1002/\(SICI\)1097-0207\(19990910\)46:1<131::AID-NME726>3.0.CO;2-J](http://dx.doi.org/10.1002/(SICI)1097-0207(19990910)46:1<131::AID-NME726>3.0.CO;2-J).
- [17] Zhang Y, Haeri S, Pan G, Zhang Y. Strongly coupled peridynamic and lattice Boltzmann models using immersed boundary method for flow-induced structural deformation and fracture. *J Comput Phys* 2021;435:110267. <http://dx.doi.org/10.1016/j.jcp.2021.110267>.
- [18] Zhang Y, Pan G, Zhang Y, Haeri S. A multi-physics peridynamics-DEM-IB-CLBM framework for the prediction of erosive impact of solid particles in viscous fluids. *Comput Methods Appl Mech Engrg* 2019;352:675–90. <http://dx.doi.org/10.1016/j.cma.2019.04.043>.
- [19] Ren H, Zhuang X, Cai Y, Rabczuk T. Dual-horizon peridynamics. *Internat J Numer Methods Engrg* 2016;108(12):1451–76. <http://dx.doi.org/10.1002/nme.5257>.
- [20] Rabczuk T, Zhuang X. Chapter 2 - dual-horizon peridynamics (DH-pd). In: Oterkus E, Oterkus S, Madenci E, editors. Peridynamic modeling, numerical techniques, and applications. Elsevier series in mechanics of advanced materials, Elsevier; 2021, p. 35–56. <http://dx.doi.org/10.1016/B978-0-12-820069-8.00021-4>.
- [21] Hu W, Ha YD, Bobaru F, Silling SA. The formulation and computation of the nonlocal J-integral in bond-based peridynamics. *Int J Fract* 2012;176(2):195–206. <http://dx.doi.org/10.1007/s10704-012-9745-8>.
- [22] Silling SA, D'Elia M, Yu Y, You H, Fermin-Coker M. Peridynamic model for single-layer graphene obtained from coarse-grained bond forces. *J Peridynamics Nonlocal Model* 2023;5(2):183–204. <http://dx.doi.org/10.1007/s42102-021-00075-w>.
- [23] Wang Y, Zhou X, Kou M. A coupled thermo-mechanical bond-based peridynamics for simulating thermal cracking in rocks. *Int J Fract* 2018;211(1–2):13–42. <http://dx.doi.org/10.1007/s10704-018-0273-z>.

- [24] Wang Y, Zhou X, Wang Y, Shou Y. A 3-D conjugated bond-pair-based peridynamic formulation for initiation and propagation of cracks in brittle solids. *Int J Solids Struct* 2018;134:89–115. <http://dx.doi.org/10.1016/j.ijsolstr.2017.10.022>.
- [25] Madenci E, Dorduncu M, Phan N, Gu X. Weak form of bond-associated non-ordinary state-based peridynamics free of zero energy modes with uniform or non-uniform discretization. *Eng Fract Mech* 2019;218:106613. <http://dx.doi.org/10.1016/j.engfracmech.2019.106613>.
- [26] Zhou X-P, Yu X-L. A vector form conjugated-shear bond-based peridynamic model for crack initiation and propagation in linear elastic solids. *Eng Fract Mech* 2021;256:107944. <http://dx.doi.org/10.1016/j.engfracmech.2021.107944>.
- [27] Nikolaev P, Sedighi M, Jivkov AP, Margetts L. Analysis of heat transfer and water flow with phase change in saturated porous media by bond-based peridynamics. *Int J Heat Mass Transfer* 2022;185:122327. <http://dx.doi.org/10.1016/j.ijheatmasstransfer.2021.122327>.
- [28] Li S, Lu H, Huang X, Qin R, Mao J. Sensitivity analysis of notch shape on brittle failure by using uni-bond dual-parameter peridynamics. *Eng Fract Mech* 2023;291:109566. <http://dx.doi.org/10.1016/j.engfracmech.2023.109566>.
- [29] Masoumi A, Salehi M, Ravandi M. A modified bond-based peridynamic model without limitations on elastic properties. *Eng Anal Bound Elem* 2023;149:261–81. <http://dx.doi.org/10.1016/j.enganabound.2023.01.030>.
- [30] Ongaro G, Shojaei A, Mossaiby F, Hermann A, Cyron CJ, Trovalusci P. Multi-adaptive spatial discretization of bond-based peridynamics. *Int J Fract* 2023;244(1):1–24. <http://dx.doi.org/10.1007/s10704-023-00709-8>.
- [31] Ren H, Zhuang X, Fu X, Li Z, Rabczuk T. Bond-based nonlocal models by nonlocal operator method in symmetric support domain. *Comput Methods Appl Mech Engrg* 2024;418:116230. <http://dx.doi.org/10.1016/j.cma.2023.116230>.
- [32] Liu Y, Han F, Zhang L. An extended fictitious node method for surface effect correction of bond-based peridynamics. *Eng Anal Bound Elem* 2022;143:78–94. <http://dx.doi.org/10.1016/j.enganabound.2022.05.023>.
- [33] Zhang J, Han F, Yang Z, Cui J. Coupling of an atomistic model and bond-based peridynamic model using an extended arlequin framework. *Comput Methods Appl Mech Engrg* 2023;403:115663. <http://dx.doi.org/10.1016/j.cma.2022.115663>.
- [34] Sun WK, Yin BB, Akbari A, Kodur VKR, Lieu KM. A coupled 3D thermo-mechanical peridynamic model for cracking analysis of homogeneous and heterogeneous materials. *Comput Methods Appl Mech Engrg* 2024;418:116577. <http://dx.doi.org/10.1016/j.cma.2023.116577>.
- [35] Huang YZ, Yu Y, Hu YL, Yao ZY, Wu D. Multi-physical analysis of ablation for c/c composites based on peridynamics. *Acta Astronaut* 2024;214:1–10. <http://dx.doi.org/10.1016/j.actaastro.2023.10.017>.
- [36] Zhou L, Zhu Z. A coupled thermo-mechanical peridynamic model for fracture behavior of granite subjected to heating and water-cooling processes. *J Rock Mech Geotech Eng* 2024;16(6):2006–18. <http://dx.doi.org/10.1016/j.jrmge.2023.07.021>.
- [37] Gu X, Li X, Xia X, Madenci E, Zhang Q. A robust peridynamic computational framework for predicting mechanical properties of porous quasi-brittle materials. *Compos Struct* 2023;303:116245. <http://dx.doi.org/10.1016/j.compstruct.2022.116245>.
- [38] Kılıç B, Madenci E. An adaptive dynamic relaxation method for quasi-static simulations using the peridynamic theory. *Theor Appl Fract Mech* 2010;53(3):194–204. <http://dx.doi.org/10.1016/j.tafmec.2010.08.001>.
- [39] Han F, Li Z. A peridynamics-based finite element method (perifem) for quasi-static fracture analysis. *Acta Mech Solida Sin* 2022;35(3):446–60. <http://dx.doi.org/10.1007/s10338-021-00307-y>.
- [40] Wang H, Wu L, Guo J, Yu C, Li Y, Wu Y. Three-dimensional modeling and analysis of anisotropic materials with quasi-static deformation and dynamic fracture in non-ordinary state-based peridynamics. *Appl Math Model* 2024;125:625–48. <http://dx.doi.org/10.1016/j.apm.2023.09.016>.
- [41] Huang D, Lu G, Qiao P. An improved peridynamic approach for quasi-static elastic deformation and brittle fracture analysis. *Int J Mech Sci* 2015;94–95:111–22. <http://dx.doi.org/10.1016/j.ijmecsci.2015.02.018>.
- [42] Zhong J, Han F, Zhang L. Accelerated peridynamic computation on GPU for quasi-static fracture simulations. *J Peridynamics Nonlocal Model* 2023;6(1):206–29. <http://dx.doi.org/10.1007/s42102-023-00095-8>.
- [43] Ma Q, Huang D, Wu L, Chen D. An improved peridynamic model for quasi-static and dynamic fracture and failure of reinforced concrete. *Eng Fract Mech* 2023;289:109459. <http://dx.doi.org/10.1016/j.engfracmech.2023.109459>.
- [44] Friedrich LF, Iturrioz I, Colpo AB, Vantadori S. Fracture failure of quasi-brittle materials by a novel peridynamic model. *Compos Struct* 2023;323:117402. <http://dx.doi.org/10.1016/j.compstruct.2023.117402>.
- [45] Chen Z, Chu X, Duan Q. A micromorphic peridynamic model and the fracture simulations of quasi-brittle material. *Eng Fract Mech* 2022;271:108631. <http://dx.doi.org/10.1016/j.engfracmech.2022.108631>.
- [46] Butti SN, Meschke G. Peridynamic analysis of dynamic fracture: influence of peridynamic horizon, dimensionality and specimen size. *Comput Mech* 2021;67(6):1719–45. <http://dx.doi.org/10.1007/s0466-021-02017-1>.
- [47] Foster JT, Silling SA, Chen WW. State based peridynamic modeling of dynamic fracture. In: SEM annual conf and exposition on experimental and applied mechanics, Albuquerque, USA. 2009, p. 2312–7.
- [48] Bobaru F. Influence of van der waals forces on increasing the strength and toughness in dynamic fracture of nanofibre networks: a peridynamic approach. *Modelling Simul Mater Sci Eng* 2007;15(5):397–417. <http://dx.doi.org/10.1088/0956-0393/15/5/002>.
- [49] Yang J, Shen Z, Zhang J, Zhao L. An improved implicit non-ordinary state-based peridynamics model for modeling crack propagation and coalescence problems. *Eng Fract Mech* 2023;292:109640. <http://dx.doi.org/10.1016/j.engfracmech.2023.109640>.
- [50] Hashim NA, Coombs WM, Augarde CE, Hattori G. An implicit non-ordinary state-based peridynamics with stabilised correspondence material model for finite deformation analysis. *Comput Methods Appl Mech Engrg* 2020;371:113304. <http://dx.doi.org/10.1016/j.cma.2020.113304>.
- [51] Li P, Hao Z, Yu S, Zhen W. Implicit implementation of the stabilized non-ordinary state-based peridynamic model. *Internat J Numer Methods Engrg* 2019;121(4):571–87. <http://dx.doi.org/10.1002/nme.6234>.
- [52] Ni T, Zaccariotto M, Zhu Q-Z, Galvanetto U. Static solution of crack propagation problems in peridynamics. *Comput Methods Appl Mech Engrg* 2019;346:126–51. <http://dx.doi.org/10.1016/j.cma.2018.11.028>.
- [53] Zaccariotto M, Luongo F, sarego G, Galvanetto U. Examples of applications of the peridynamic theory to the solution of static equilibrium problems. *Aeronaut J* 2016;119(1216):677–700. <http://dx.doi.org/10.1017/s0001924000010770>.
- [54] Brothers MD, Foster JT, Millwater HR. A comparison of different methods for calculating tangent-stiffness matrices in a massively parallel computational peridynamics code. *Comput Methods Appl Mech Engrg* 2014;279:247–67. <http://dx.doi.org/10.1016/j.cma.2014.06.034>.
- [55] Breitenfeld MS, Geubelle PH, Weckner O, Silling SA. Non-ordinary state-based peridynamic analysis of stationary crack problems. *Comput Methods Appl Mech Engrg* 2014;272:233–50. <http://dx.doi.org/10.1016/j.cma.2014.01.002>.
- [56] Mace RW, Silling SA. Peridynamics via finite element analysis. *Finite Elem Anal Des* 2007;43(15):1169–78. <http://dx.doi.org/10.1016/j.finel.2007.08.012>.
- [57] Bezanson J, Edelman A, Karpinski S, Shah VB. Julia: A fresh approach to numerical computing. *SIAM Rev* 2017;59(1):65–98. <http://dx.doi.org/10.1137/141000671>.
- [58] Ren H, Zhuang X, Rabczuk T. A nonlocal operator method for solving partial differential equations. *Comput Methods Appl Mech Engrg* 2020;358:112621. <http://dx.doi.org/10.1016/j.cma.2019.112621>.
- [59] Altay U, Dorduncu M, Kadioglu S. An improved peridynamic approach for fatigue analysis of two dimensional functionally graded materials. *Theor Appl Fract Mech* 2023;128:104152. <http://dx.doi.org/10.1016/j.tafmec.2023.104152>.
- [60] Dipasquale D, Sarego G, Zaccariotto M, Galvanetto U. Dependence of crack paths on the orientation of regular 2D peridynamic grids. *Eng Fract Mech* 2016;160:248–63. <http://dx.doi.org/10.1016/j.engfracmech.2016.03.022>.